

Research Article

Magnetic-Mixed Convection in Nanofluid-Filled Cavity Containing Baffles and Rotating Hollow-Cylinders with Roughness Components

Mohammad Mokaddes Ali ¹, Rowsanara Akhter ², Md. Abdul Alim ³,
and Md. Musa Miah ¹

¹Department of Mathematics, Mawlana Bhashani Science and Technology University, Tangail 1902, Bangladesh

²Department of Natural Sciences, The International University of Scholars, Dhaka 1213, Bangladesh

³Department of Mathematics, Bangladesh University of Engineering and Technology, Dhaka 1000, Bangladesh

Correspondence should be addressed to Mohammad Mokaddes Ali; mmali309.math@mbstu.ac.bd

Received 23 August 2022; Revised 30 October 2022; Accepted 21 November 2022; Published 14 December 2022

Academic Editor: Sardar Muhammad Bilal

Copyright © 2022 Mohammad Mokaddes Ali et al. This is an open access article distributed under the Creative Commons Attribution License, which permits unrestricted use, distribution, and reproduction in any medium, provided the original work is properly cited.

Mixed convective heat transfer in a nanofluid-filled lid-driven square cavity equipped with a rotating cylinder, horizontal baffles, and an external magnetic field is numerically examined in this study. A cylinder with triangular components is set at the centre of the cavity while two horizontal baffles are fixed to its vertical walls. The cavity is under the impact of the external magnetic field. Modified Maxwell's model is taken into consideration to estimate the thermal conductivity of nanofluids. Galerkin FEM is applied to simulate nondimensional governing equations. The computations are carried out for specific ranges of physical parameters, and the results are illustrated through streamlines, isotherms, and average Nusselt number bar charts. Contours plotting indicate that flow circulation and distribution of temperature are significantly affected by the speed of a rotating rough cylinder. The fluid velocity remarkably increases with an increase in speed ratio and Reynolds number but it declines with Hartmann number, baffle length, and volume fraction. Heat transfer rate is substantially augmented by increasing the rotational speed of the rough cylinder, heights of triangular components, and suspended-nanoparticles which are also optimized for increasing baffle's length and its horizontal arrangement. The findings of this investigation can be applied to improve the cooling efficiency of engineering equipment such as heat exchangers, energy storage systems, electronic equipment, solar collectors, and nuclear reactor safety devices.

1. Introduction

Convective heat transfer in confined enclosures is of great interest to the engineers and researchers as it is frequently encountered in heat transport processes in various engineering fields such as heat exchangers, electronic cooling, energy storage systems, solar technologies, and nuclear reactor systems. Among the heat transfer processes, convective heat transfer is a complex phenomenon which is developed by the interaction of thermal buoyancy flow caused by temperature differences and shear flow caused by additional forces such as moving surfaces, rotating surfaces, or inlet-outlet flow. In addition, heat transfer associated with magnetic fields has taken researcher's attention considering

its extensive applications in engineering, for example, crystal growth in liquid, electronic packaging, solar technology, nuclear reactor cooling, molten metal purification, and petroleum industry. In this case, magnetic force interacts with the buoyancy flow and produces Lorentz force which influences the fluid flow and heat transport mechanisms. Recently, researchers found limitations in using convective liquids such as water, oil, and ethylene glycol as coolants named lower thermal conductivity. They have tried to break down this limitation and developed novel heat transfer fluids by amalgamating nanoparticles in different base fluids named nanofluids which have superior properties such as higher thermal conductivity, improved stability, minimal clogging in the flow domain, and reduced pumping

power. In this context, many researchers and engineers were interested in accomplishing their theoretical and experimental studies of natural convection/mixed convection/forced convection in different configurations filled with different nanofluids under the influence of the magnetic field or in absence of magnetic field. Some of the related studies have been presented here.

Fereidoon et al. [1] investigated mixed convection in a double lid-driven square cavity by using the finite volume method and recommended that heat transfer increases with solid volume fraction at a fixed Reynolds number. They also noted that it is increased for Ri and Re at a fixed solid volume fraction. Later on, Muthtamilselvan and Doh [2] conducted a similar study considering the magnetic field effect in the vertical direction and found the flow, heat, and mass transfer characteristics strongly depends on the magnetic field strength. Ismael et al. [3] examined the effects of partial slip and inclined magnetic field on mixed convection and showed that the convection due to partial slip is controlled with the strength and orientation of the magnetic field. Kasaeipoor et al. [4] utilized a finite volume approach to study mixed convection in a T-shaped cavity under the magnetic field effect. They demonstrated the heat transfer in nanofluid increases while the cavity aspect ratio was increased. Kefayati [5] used Buongiorno's mathematical model to investigate mixed convection in nonNewtonian nanofluid flow and observed heat and mass transfer enhance with the buoyancy ratio number, whereas mass transfer ameliorated with thermophoresis and Brownian motion. Öztop et al. [6] investigated mixed convection in a wavy-walled cavity filled by nanofluid and noted that enhancement of heat transfer for volume fraction depends on Ha and Ri . Armaghani et al. [7] studied natural convection in a nanofluid-filled baffled L-shaped cavity. In their study, finite volume method was implemented and found heat transfer increasing with the aspect ratio and baffles length. Karimdoost Yasuri et al. [8] conducted similar analysis in a square cavity with a baffle and an external magnetic field. They recorded that heat transfer increases for increasing Ra and baffles length but decreases for Ha . After that, Hussein et al. [9] numerically investigated natural convection in inclined cavity having a cold baffle filled by Al_2O_3 /water nanofluid and found Nusselt number increases with Ra and ϕ , but it decreases with the cavity aspect ratio and inclination angle. Ziam et al. [10] proposed a single-phase nanofluid model to analyze natural convection in a baffled U-shaped cavity. They considered Brinkman and Wasp models and suggested heat transfer rate increases for increased Ra and ϕ but diminishes for Ha . Aljabair et al. [11] used FORTRAN code to solve mixed convection in a nonuniformly heated arc-shaped cavity. They recommended the local and average Nusselt numbers are increasing function of ϕ , Re , and Ra . They also presented numerical results based on correlation equations for the average Nusselt number. Al-Farhany et al. [12] studied magnetohydrodynamic natural convection in an inclined porous cavity with conducting horizontal fins and showed the highest length and the widest gap of the fins cause superior heat transfer situation within the cavity. Shah et al. [13] analyzed the magnetized viscous fluid flow of a

water-based hybrid nanofluid containing single-wall carbon nanotubes through a permeable channel by implementing a nanolayer approach and demonstrated that heat flux increases by the induction of single-wall carbon nanotubes in water, and the nanolayer as well as the particle radius causes an enhancement in the thermal conductance of the base fluid. Bilal et al. [14] investigated natural convection flow of power-law fluids in trapezoidal cavity with a nonuniformly U-shaped fin by using the finite element method and COMSOL Multiphysics software (5.6) and highlighted that heat transportation and momentum profile increase with the increase in the Rayleigh number which decline for increased viscosity of the fluid. After that, Bilal et al. [15] performed a similar investigation for a square cavity with nonuniformly T-shaped fin. Later on, Shah et al. [16] studied natural convection flow of power-law fluids an isosceles triangular cavity by using similar software and found noticeable influence of governing parameters on local and average heat flux coefficients and kinetic energy. It was also inferred that a higher Rayleigh number causes enrichment in local heat transfer and kinetic energy, whereas the reverse phenomenon occurs for the power-law index. Another numerical study [17] pointed out that more heat transfer is achieved with the addition of metallic particles to base fluid compared to nonmetallic particles. Moreover, an elevated Nusselt number is found for increasing the magnitude of nanoparticle volume fraction, but it depreciates the skin friction coefficient. Qureshi et al. [18] optimized entropy generation for the induction of hybrid magnetized nanoparticles between two coaxially rotating porous disks and showed that entropic generation is reduced with upsurge in inducted hybridized particles volume fraction and Bejam number is found inversely related with entropy generation. After that, Qureshi et al. [19] examined three-dimensional triadic hybrid nanofluid flow between two coaxially rotating disks with magnetic field effects and found that hybrid nanofluids containing $Cu-Al_2O_3$ nanoparticles showed significantly better results than those of other hybrid nanoparticles. It was also recorded that the thermal conductance of nanofluids is directly correlated with the morphology of any hybrid nanoparticles. Bilal et al. [20] considered the Cattaneo-Christov heat flux model and transverse magnetic field to analyze heat transfer of Williamson fluid flow over an exponentially stretched the surface by shooting and Runge-Kutta-method and showed that the velocity field is suppressed by the magnetic field and Williamson fluid parameter. Later on, Bilal et al. [21] performed finite difference simulations of viscous fluid flow over a permeable rotating disk to explore the flow in the presence of the transverse magnetic field and recommended that the tangential and radial velocity components are enhanced with the magnetic strength parameter, whereas the opposite trend occurred in the axially directed velocity. The flow and thermal fields within simple geometrical models with/without baffles or fins were numerically explored in these studies [1–21] by using different nanofluids in the presence of the magnetic field or not. It needs to be highlighted that geometrical configuration with appropriate obstruction was not considered in those investigations.

Insertion of detached obstructions of various shapes such as circular, square, tilted-square, and triangular has an impact on controlling fluid flow and heat transfer characteristics inside confined enclosures where fluid flow needs to be restricted or bifurcated. Thus, configurations with appropriate obstructions can significantly affect the flow and temperature fields compared to other simple shapes. A large number of studies have been conducted considering these phenomena. Rahman et al. [22] investigated mixed convection in a rectangular cavity with a circular cylinder and pointed out that the dimensionless temperature and heat transfer were strongly dependent on the dimensionless parameters and configurations studied. Majdi et al. [23] used the Fluent 6.3 commercial program to analyze combined convection in a triangular cavity with an insulated cylinder. They illustrated that heat transfer rate is enhanced with the volume fraction of nanoparticles but it decreases with Ri . Ishak et al. [24] studied mixed convection in a trapezoidal cavity having a solid cylinder and filled with nanofluids containing Al_2O_3 nanoparticles. Their results showed the heat transfer and Bejan number improved with the location and size of the solid cylinder. Aly et al. [25] used the ISPH method to investigate mixed convection in a lid-driven cavity with circular cylinders in motion and suggested that the SPH tool can be applied easily to solve complicated 2D and 3D problems. Bilal et al. [26] analyzed the flow and heat transfer of nonlinear fluid in a square cavity with a cold cylinder and revealed that convective heat transfer and kinetic energy arise for Ra but decrease for the power-law index. The problem of heat transportation of mixed convection in Newtonian fluid enclosed by square cavity with a placement of adiabatic square cylinder was investigated by Khan et al. [27] and revealed that increased Reynolds number causes decrement in kinetic energy of fluid, whereas thermal buoyancy forces and Nusselt number increase for increasing Grashof number. Shah et al. [28] examined the heat and mass transportation of double diffusive natural convection in Casson non-Newtonian fluid enclosed by a hexagonal enclosure with an isothermally heated cylinder in the presence of an inclined magnetic field by practicing COMSOL Multiphysics software and found that heat and mass flux coefficients diminish for the magnetic field effect, whereas heat and mass flux distribution are found upsurging with a Casson fluid parameter. Bansal and Chatterjee [29] performed a numerical study of magneto-convective flow in a lid-driven cavity that included a rotating and heat conducting cylinder. In their study, the flow and thermal fields were found qualitatively change with mixed convective strength, magnetic field, and concentration of nanoparticles. Another numerical study [30] pointed out 14.2% more heat transfer in a rotating state compared to a motionless state. Later on, Malla et al. [31] studied a similar problem considering a fluid-porous layer using ANSYS fluent software, and a stable system was found at lower Da and minimum heat transfer at about $Ri = 10$. Ali et al. [32] numerically analyzed the flow and heat transfer in mixed convection

through grooved channels, and they noticed the flow and heat transfer mechanisms, due to governing parameters, are more effective with the presence of a rotating heat source. Al-Kouz et al. [33] investigated irreversibilities and heat transfer of mixed convection in wavy enclosure containing a rotating cylinder and showed the flow function and heat transfer enhancement become maximum at increasing Ra . Thus, it is clearly seen that fluid motion and temperature distribution inside a cavity are influenced by the presence of internal blockage. However, irregular surfaces of internal blockage were not considered in these studies, but they can be used to improve or control the flow function and heat transfer enhancement in a closed or open cavity.

The irregular surfaces, either static or in motion, of a geometrical configuration generate contributory recirculating regions that can enhance flow mixing within the cavity and heat transfer compared to other smooth configurations. Thus, such complicated configurations can cause substantial improvement in the heat transfer performance and flow mixing and play significant roles in engineering processes such as heat exchangers, electronic cooling systems, solar technologies, nuclear reactors, lubrication systems, and chemical processing equipment. Based on this idea, many studies have been accomplished by the researchers. Gangawane and Manikandan [34] studied natural convection in a square cavity containing a hexagonal block with different thermal conditions and demonstrated the flow and temperature pattern changes were remarkable for both thermal conditions. It was also found that heat transfer decreases with the power-law index. Sheikholeslami et al. [35] investigated transportation of nanoparticles in a circular porous cavity with complex inner shaped in the presence of magnetic force and illustrated nanofluid motion that decreases with the magnetic force, and the Nusselt number increases for reducing cavity porosity. Later on, Alhashash [36] accomplished a similar study considering a square cavity with a hot corrugated cylinder and recommended that heat transfer from a corrugated cylinder is better than a smooth cylinder under specific circumstances. Tayebi and Chamkha [37] carried out parametric analysis of natural convection in a nanofluid field enclosure with a wavy cylinder and pointed out that flow and heat transfer characteristics are controlled by the presence of a wavy conductive cylinder. Ismael [38] utilized a finite difference method to examine mixed convection in an enclosure with an arc-shaped moving wall and showed that heat transfer due to rotational speed is irrespective at lower Ra but significant at higher Ra . Ali et al. [39] numerically investigated mixed convection in a concentric rotating cylinder and an inner sinusoidal cylinder. In their study, COMSOL 5.2a was used to solve the modeled governing equations and illustrated the formation of stream and temperature lines, as well as how the Nusselt number was affected by the number of corrugations of the inner cylinder and the governing parameters studied. Hamzal et al. [40] analyzed the mixed convection of a rotating cylinder immersed in a nanofluid-filled cavity

associated with a magnetic field and heat flux. They concluded the enhancement of heat transfer processes for NPs volume fraction, which is promoted with increasing Ra.

Based on the presented literature review, it is evident that mixed convective heat transfer in the presence of a magnetic field is of considerable interest for researchers and engineers and is applicable in science and engineering fields. A lot of research has been conducted for mixed convection in different geometries filled with different fluids. Though mixed convection in different geometries is considered in the open literature, mixed convective heat transfer in a lid-driven nanofluid-filled partially heated cavity having a rotating cylinder with roughness components in the presence of baffles has never been investigated. But it has a significant influence to improve the heat transfer efficiency by enhancing the effective flow circulation due to the presence of roughness components and nanofluid thermal conductivity and is more applicable in engineering fields. Accordingly, authors have been interested to examine the fluid flow and heat transfer behaviours in a nanofluid-filled partially heated cavity equipped by centred rotating cylinder with roughness components and moving top wall and also a pair of baffles attached to the cavity vertical walls under the influence of transverse magnetic field. As per literature survey and author's knowledge, no such work was reported yet. Galerkin's finite element method is utilized to simulate the modified governing equations in this study. The numerical results are obtained for different physical parameters and explained via streamlines, isotherms, and average Nusselt number bar charts. This type of configuration may be set up in engineering equipment such as high-performance heat exchangers, energy storage systems, cooling of electronic equipment, solar collectors, space thermal management, and reactor safety devices.

2. Physical Model

Figure 1 represents the geometrical configuration of a two-dimensional square cavity of length L . A pair of horizontal baffles of 20% cavity length is fixed to the vertical walls of the cavity, and a circular obstacle of radius R ($=10\% L$) with triangular roughness components is positioned at its centre which is rotated at angular velocity ω . The free region between the cavity and the obstacle is filled with alumina water nanofluid that is heated partially from the cavity bottom wall and cooled from its top moving wall at a uniform velocity U_0 . Remaining walls and baffles are maintained no-slip condition and kept

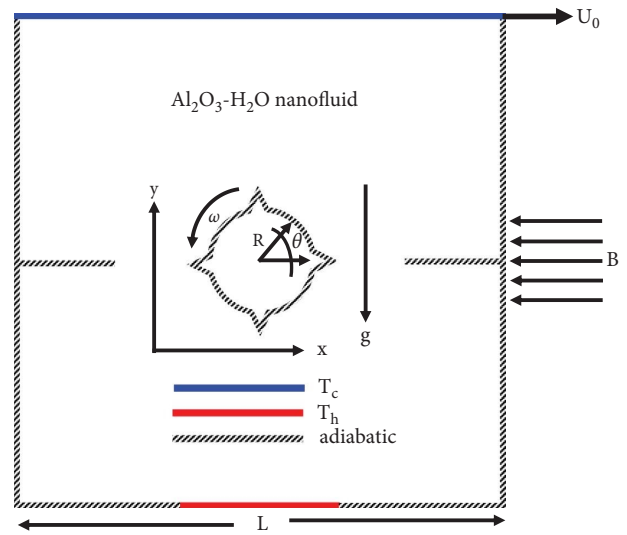


FIGURE 1: Physical model of the present study.

adiabatic. The mixed convection is induced due to the rotating rough cylinder and top moving wall along with temperature differences of the active thermal condition. A uniform magnetic field affects the flow field, and gravitational acceleration is also activated in the downward direction. The thermophysical properties of nanoparticles and water are available in [41, 42].

3. Mathematical Analysis

The vector form of conservation equations representing the flow model is defined considering the Boussinesq approximation and the described physical model as follows [29, 42–44]:

$$\nabla \cdot V = 0, \quad (1)$$

$$V \cdot \nabla V = -\frac{1}{\rho_{nf}} \nabla p + \nu_{nf} \nabla^2 V + F, \quad (2)$$

$$V \cdot \nabla T = a_{nf} \nabla^2 T. \quad (3)$$

The source terms used in the governing equation (2) are presented in Table 1.

The used properties of nanofluid are as follows [30, 32, 41, 42, 45–48]:

TABLE 1: Elaboration of source terms [43, 44].

F	$(1/\rho_{nf})I \times \bar{B} - \bar{g}\beta_{nf}(T - T_c): I$	$\sigma_{nf}(-\nabla\varphi + V \times B)$ and $\nabla^2 \cdot \varphi = 0$
-----	---	---

$$\begin{aligned} \rho_{nf} &= (1 - \phi)\rho_{bf} + \phi\rho_{np}, \\ (\rho c_p)_{nf} &= (1 - \phi)(\rho c_p)_{bf} + \phi(\rho c_p)_{np}, \\ \beta_{nf} &= (1 - \phi)\beta_{bf} + \phi\beta_{np}, \\ \sigma_{nf} &= \frac{\sigma_{bf} 1 + 3\sigma_{np}/\sigma_{bf} - 1\phi}{((\sigma_{np}/\sigma_{bf} + 2 - \sigma_{np}/\sigma_{bf} - 1\phi))}, \\ \mu_{nf} &= \mu_{bf}(1 + 39.11\phi + 533.9\phi^2), \\ k_{nf} &= \frac{(k_{np} + 2k_{bf} - 2\phi(k_{bf} - k_{np}))}{(k_{np} + 2k_{bf} + \phi(k_{bf} - k_{np}))}k_f + \frac{\phi\rho_{np}c_{p,np}}{2}\sqrt{\frac{K_B T_{ref}}{3\pi d_{np}\mu_{bf}}}. \end{aligned} \tag{4}$$

Corresponding boundary conditions based on the physical model are specified as follows:

On the top wall: $V = (U_0, 0), T = T_c,$

$$\text{On the bottom wall: } V = 0, \begin{cases} \nabla T \cdot n = 0 \text{ when } x < \frac{L}{3} \text{ and } x > \frac{2L}{3} \\ T = T_h \text{ when } \frac{L}{3} \leq x \leq \frac{2L}{3} \end{cases}, \tag{5}$$

On the vertical walls and baffles: $V = 0$ and $\nabla T \cdot n = 0,$

On the on the cylinder: $V_c = \left(\frac{V_p}{U_0} \sin \theta, \frac{V_p}{U_0} \cos \theta\right)$ and $\nabla T \cdot n = 0,$ where $V_p = \omega R$ and $0 \leq \theta \leq 2\pi.$

$$\nabla \cdot V^* = 0, \tag{7}$$

The dimensionless variables in equation (6) are introduced in the governing equations to make its dimensionless form:

$$(x^*, y^*) = \frac{(x, y)}{L}, V = V^*U_0, p = p^*\rho_{nf}U_0^2 \text{ and } \theta^* = \frac{(T - T_c)}{(T_h - T_c)}, \tag{6}$$

$$\begin{aligned} V^* \cdot \nabla V^* &= -\nabla p^* + \left(\frac{\nu_{nf}}{\nu_{bf}}\right) \\ &\cdot \left(\frac{1}{Re}\right)\nabla^2 V^* + F^*, \end{aligned} \tag{8}$$

and which are

$$V^* \cdot \nabla \theta^* = \left(\frac{\alpha_{nf}}{\alpha_{bf}}\right)\left(\frac{1}{(Re \ Pr)}\right)\nabla^2 \theta^*. \tag{9}$$

The modified form of the source terms of Table 1 and equation (8) are provided in the following Table 2.

With the help of equation (6), the dimensionless boundary conditions (shown in equation (5)) are written as the following:

On the top wall: $V^* = (1, 0), \theta^* = 0,$

$$\text{On the bottom wall: } V^* = 0, \left\{ \begin{array}{l} \nabla \theta^* \cdot n = 0 \text{ when } x^* < \frac{L}{3} \text{ and } x^* > \frac{2L}{3} \\ \theta^* = 1, \text{ when } \frac{L}{3} \leq x^* \leq \frac{2L}{3} \end{array} \right. , \quad (10)$$

On the vertical walls and baffles: $V^* = 0, \nabla \theta^* \cdot n = 0,$

On the on the cylinder: $V_c^* = (Sr \sin \theta, Sr \cos \theta)$ and $\nabla \theta^* \cdot n = 0$ where $Sr = \frac{V_p}{U_0}$.

3.1. Evaluation of Average Nusselt Number. The local Nusselt number is computed at the heated midsectional wall of the cavity, which is defined in nondimensional form as follows [51, 52]:

$$Nu = \frac{k_{mf}}{k_{bf}} \frac{\partial \theta^*}{\partial y^*}, \quad (11)$$

and corresponding average Nusselt number is estimated as follows [51, 52]:

$$\bar{Nu} = \frac{1}{L_T} \int_{L/3}^{2L/3} Nu \, dx^* \text{ where } L_T = \frac{2L}{3} - \frac{L}{3}, \quad (12)$$

3.2. Numerical Procedure. The numerical simulation of the governing equations (7)–(9) along with the boundary conditions 10a-d has been performed using Galerkin weighted finite element method. In this simulation procedure, the governing partial differential equations are converted into integral equations by implementing the Galerkin weighted residual method [53]. The obtained integral equations are as follows:

$$\int_A N_\alpha \left(\frac{\partial U}{\partial X} + \frac{\partial V}{\partial Y} \right) dA = 0, \quad (13)$$

$$\int_A N_\alpha \left(U \frac{\partial U}{\partial X} + V \frac{\partial U}{\partial Y} \right) dA = - \int_A H_\lambda \frac{\partial P}{\partial X} dA + \left(\frac{\nu_{nf}}{\nu_{bf}} \right) \left(\frac{1}{Re} \right) \int_A N_\alpha \left(\frac{\partial^2 U}{\partial X^2} + \frac{\partial^2 U}{\partial Y^2} \right) dA, \quad (14)$$

$$\begin{aligned} \int_A N_\alpha \left(U \frac{\partial V}{\partial X} + V \frac{\partial V}{\partial Y} \right) dA = & - \int_A H_\lambda \frac{\partial P}{\partial Y} dA + \left(\frac{\nu_{nf}}{\nu_{bf}} \right) \left(\frac{1}{Re} \right) \int_A N_\alpha \left(\frac{\partial^2 V}{\partial X^2} + \frac{\partial^2 V}{\partial Y^2} \right) dA \\ & + \left(\frac{\beta_{nf}}{\beta_{bf}} \right) \left(\frac{Gr}{Re^2} \right) \int_A N_\alpha \theta dA - \left(\frac{\rho_{bf}}{\rho_{nf}} \right) \left(\frac{\sigma_{nf}}{\sigma_{bf}} \right) \left(\frac{Ha^2}{Re} \right) \int_A N_\alpha V dA, \end{aligned} \quad (15)$$

$$\int_A N_\alpha \left(U \frac{\partial \theta}{\partial X} + V \frac{\partial \theta}{\partial Y} \right) dA = \left(\frac{\alpha_{nf}}{\alpha_{bf}} \right) \left(\frac{1}{Pr Re} \right) \int_A N_\alpha \left(\frac{\partial^2 \theta}{\partial X^2} + \frac{\partial^2 \theta}{\partial Y^2} \right) dA. \quad (16)$$

Here, A is the element area, N_α ($\alpha = 1, 2, \dots, 6$) are the element shape functions or interpolation functions for the velocity components and temperature, and H_λ ($\lambda = 1, 2, 3$) are the element shape functions for the pressure. The Gaussian

divergence theorem has been introduced in equations (13)–(16). to generate the boundary integral terms associated with the surface tractions and heat flux in the momentum and energy equations and we obtained the following equations:

TABLE 2: Source terms are [43, 44, 49, 50].

F_{x^*}	0
F_{y^*}	$(\beta_{nf}/\beta_{bf})(Gr/Re^2)\theta^* - (\rho_{bf}/\rho_{nf})(\sigma_{nf}/\sigma_{bf})(Ha^2/Re)V^*$

$$\int_A N_\alpha \left(\frac{\partial U}{\partial X} + \frac{\partial V}{\partial Y} \right) dA = 0, \quad (17)$$

$$\int_A N_\alpha \left(U \frac{\partial U}{\partial X} + V \frac{\partial U}{\partial Y} \right) dA + \int_A H_\lambda \frac{\partial P}{\partial X} dA - \left(\frac{\nu_{nf}}{\nu_{bf}} \right) \left(\frac{1}{Re} \right) \int_A \left(\frac{\partial N_\alpha}{\partial X} \frac{\partial U}{\partial X} + \frac{\partial N_\alpha}{\partial Y} \frac{\partial U}{\partial Y} \right) dA = \int_{A_0} N_\alpha A_x dA_0 \quad (18)$$

$$\begin{aligned} & \int_A N_\alpha \left(U \frac{\partial V}{\partial X} + V \frac{\partial V}{\partial Y} \right) dA + \int_A H_\lambda \frac{\partial P}{\partial Y} dA - \left(\frac{\nu_{nf}}{\nu_{bf}} \right) \left(\frac{1}{Re} \right) \int_A \left(\frac{\partial N_\alpha}{\partial X} \frac{\partial V}{\partial X} + \frac{\partial N_\alpha}{\partial Y} \frac{\partial V}{\partial Y} \right) dA \\ & - \left(\frac{\beta_{nf}}{\beta_{bf}} \right) \left(\frac{Gr}{Re^2} \right) \int_A N_\alpha \theta dA + \left(\frac{\rho_{bf}}{\rho_{nf}} \right) \left(\frac{\sigma_{nf}}{\sigma_{bf}} \right) \left(\frac{Ha^2}{Re} \right) \int_A N_\alpha V dA = \int_{A_0} N_\alpha A_y dA_0, \end{aligned} \quad (19)$$

$$\int_A N_\alpha \left(U \frac{\partial \theta}{\partial X} + V \frac{\partial \theta}{\partial Y} \right) dA - \left(\frac{\alpha_{nf}}{\alpha_{bf}} \right) \left(\frac{1}{Pr Re} \right) \int_A \left(\frac{\partial N_\alpha}{\partial X} \frac{\partial \theta}{\partial X} + \frac{\partial N_\alpha}{\partial Y} \frac{\partial \theta}{\partial Y} \right) dA = \int_{A_w} N_\alpha q_w dA_w, \quad (20)$$

where the surface tractions (A_x, A_y) along the outflow boundary A_0 and velocity components and fluid temperature or heat flux (q_w) that flows into or out from the domain along the wall boundary A_w . The basic unknown for the above differential equations is the velocity components (U, V), temperature θ , and the pressure P . For the development of the finite element equations, the six-node triangular element is used in this work. All six nodes are associated with velocities as well as temperature, only the three corner nodes are linked with pressure. This means that a lower order polynomial is chosen for pressure and which is satisfied through the continuity equation. The velocity components, temperature profiles, and linear interpolation for the pressure distribution according to their highest derivative orders for the differential equations (7) to (9) are as follows:

$$U(X, Y) = N_\beta U_\beta, \quad (21)$$

$$V(X, Y) = N_\beta V_\beta, \quad (22)$$

$$\theta(X, Y) = N_\beta \theta_\beta, \quad (23)$$

$$P(X, Y) = H_\lambda P_\lambda, \quad (24)$$

where $\beta = 1, 2, \dots, 6$ and $\lambda = 1, 2, 3$. Substituting the element velocity component distributions, temperature distributions, particles distributions, and the pressure distribution from equations (21)–(24) into the equations (17)–(20), the finite element equations can be written in the following form:

$$U_\beta \int_A N_\alpha N_{\beta,x} dA + V_\beta \int_A N_\alpha N_{\beta,y} dA = 0, \quad (25)$$

$$\begin{aligned} & U_\beta U_\gamma \int_A N_\alpha N_\beta N_{\gamma,x} dA + V_\beta U_\gamma \int_A N_\alpha N_\beta N_{\gamma,y} dA + P_\mu \int_A H_\lambda H_{\mu,x} dA \\ & - \left(\frac{\nu_{nf}}{\nu_{bf}} \right) \left(\frac{1}{Re} \right) U_\beta \int_A (N_{\alpha,x} N_{\beta,x} + N_{\alpha,y} N_{\beta,y}) dA = \int_{A_0} N_\alpha A_x dA_0, \end{aligned} \quad (26)$$

$$\begin{aligned} & U_\beta V_\gamma \int_A N_\alpha N_\beta N_{\gamma,x} dA + V_\beta V_\gamma \int_A N_\alpha N_\beta N_{\gamma,y} dA + P_\mu \int_A H_\lambda H_{\mu,y} dA - \left(\frac{\nu_{nf}}{\nu_{bf}} \right) \left(\frac{1}{Re} \right) V_\beta \int_A (N_{\alpha,x} N_{\beta,x} + N_{\alpha,y} N_{\beta,y}) dA \\ & - \left(\frac{\beta_{nf}}{\beta_{bf}} \right) \left(\frac{Gr}{Re^2} \right) \theta_\beta \int_A N_\alpha N_\beta dA + \left(\frac{\rho_{bf}}{\rho_{nf}} \right) \left(\frac{\sigma_{nf}}{\sigma_{bf}} \right) \left(\frac{Ha^2}{Re} \right) V_\beta \int_A N_\alpha N_\beta dA = \int_{A_0} N_\alpha A_y dA_0, \end{aligned} \quad (27)$$

$$U_\beta \theta_\gamma \int_A N_\alpha N_\beta N_{\gamma,x} dA + V_\beta \theta_\gamma \int_A N_\alpha N_\beta N_{\gamma,y} dA - \left(\frac{\alpha_{nf}}{\alpha_{bf}} \right) \left(\frac{1}{\text{Pr Re}} \right) \theta_\beta \int_A (N_{\alpha,x} N_{\beta,x} + N_{\alpha,y} N_{\beta,y}) dA = \int_{A_w} N_\alpha q_w dA_w. \quad (28)$$

Now, we consider the coefficients in the above governing equations as follows:

$$\begin{aligned} K_{\alpha\beta^x} &= \int_A N_\alpha N_{\beta,x} dA, \\ K_{\alpha\beta^y} &= \int_A N_\alpha N_{\beta,y} dA, \\ K_{\alpha\beta\gamma^x} &= \int_A N_\alpha N_\beta N_{\gamma,x} dA, \\ K_{\alpha\beta\gamma^y} &= \int_A N_\alpha N_\beta N_{\gamma,y} dA, \\ K_{\alpha\beta} &= \int_A N_\alpha N_\beta dA, \\ S_{\alpha\beta^{xx}} &= \int_A N_{\alpha,x} N_{\beta,x} dA, \\ S_{\alpha\beta^{yy}} &= \int_A N_{\alpha,y} N_{\beta,y} dA, \\ M_{\lambda\mu^x} &= \int_A H_\lambda H_{\mu,x} dA, \\ M_{\lambda\mu^y} &= \int_A H_\lambda H_{\mu,y} dA, \\ S_{\alpha\beta^x\gamma^x} &= \int_A N_\alpha N_{\beta,y} N_{\gamma,x} dA, \\ S_{\alpha\beta^y\gamma^y} &= \int_A N_\alpha N_{\beta,y} N_{\gamma,y} dA, \\ Q_{\alpha^u} &= \int_{A_0} N_\alpha A_x dA_0, \\ Q_{\alpha^v} &= \int_{A_0} N_\alpha A_y dA_0, \\ Q_{\alpha^\theta} &= \int_{A_w} N_\alpha q_w dA_w. \end{aligned} \quad (29)$$

These element matrices are evaluated in closed form for numerical simulation. Details of the derivation for these element matrices are omitted for brevity.

With the help of the above coefficients, the finite element equations can be written in the following type:

$$K_{\alpha\beta^x} U_\beta + K_{\alpha\beta^y} V_\beta = 0, \quad (30)$$

$$K_{\alpha\beta\gamma^x} U_\beta U_\gamma + K_{\alpha\beta\gamma^y} V_\beta V_\gamma + M_{\lambda\mu^x} P_\mu - \left(\frac{\nu_{nf}}{\nu_{bf}} \right) \left(\frac{1}{\text{Re}} \right) U_\beta (S_{\alpha\beta^{xx}} + S_{\alpha\beta^{yy}}) = Q_{\alpha^u}, \quad (31)$$

$$\begin{aligned} K_{\alpha\beta\gamma^x} U_\beta V_\gamma + K_{\alpha\beta\gamma^y} V_\beta V_\gamma + M_{\lambda\mu^y} P_\mu - \left(\frac{\nu_{nf}}{\nu_{bf}} \right) \left(\frac{1}{\text{Re}} \right) V_\beta (S_{\alpha\beta^{xx}} + S_{\alpha\beta^{yy}}) - \left(\frac{\beta_{nf}}{\beta_{bf}} \right) \left(\frac{\text{Gr}}{\text{Re}^2} \right) K_{\alpha\beta\theta_\beta} \\ + \left(\frac{\rho_{bf}}{\rho_{nf}} \right) \left(\frac{\sigma_{nf}}{\sigma_{bf}} \right) \left(\frac{Ha^2}{\text{Re}} \right) K_{\alpha\beta} V_\beta = Q_{\alpha^v}, \end{aligned} \quad (32)$$

$$K_{\alpha\beta\gamma^x}U_\beta\theta_\gamma + K_{\alpha\beta\gamma^y}V_\beta\theta_\gamma - \left(\frac{\alpha_{nf}}{\alpha_{bf}}\right)\left(\frac{1}{\text{Pr Re}}\right)\theta_\beta(S_{\alpha\beta^{xx}} + S_{\alpha\beta^{yy}}) = Q_{\alpha^\theta}. \quad (33)$$

Using Newton–Raphson method explained by Reddy [54], the obtained nonlinear equations (29) to (32) are converted into linear algebraic equations. Finally, these linear equations are solved by employing the triangular factorization method and reduced integration method expressed by Zeinkiewicz et al. [55]. The convergence criterion of the numerical solution along with error estimation has been set to $|\varphi^{m+1} - \varphi^m| \leq 10^{-5}$, where m is the number of iteration and φ is a function of U , V , and θ . The details of the computational procedure are also available in the earlier studies [32, 56, 57], which are well described in [58, 59]. The simple algorithm of this study is exposed through the following flowchart (in Figure 2):

3.3. Mesh Generation. In two-dimensional configurations, mesh generation is a procedure of subdivision of the geometrical domain considering elements as triangular or quadrilateral called finite elements. These elements are connected to their neighbouring elements using characteristic points known as “nodes”. The required values of the physical quantities of a problem are calculated at every node. Meshing a complicated geometry into a significant number of elements is essential to the numerical simulations, which makes the FEM a powerful tool for solving engineering problems encountered in practical applications. The mesh configuration with triangular elements of this study is presented in Figure 3.

3.4. Grid Sensitivity Test. A grid sensitivity test is performed to acquire a grid-irrespective solution. In this regard, the average Nusselt number has been estimated at different mesh systems, and five of them have been presented in Table 3 and Figure 4 which confirm that further meshing has very small impacts on the computed average Nusselt number. Based on the presented mesh configurations with an average Nusselt number, it can be decided that meshing with 24444 nodes and 47648 elements is appropriate for an accurate solution of this study.

3.5. Validation of Computational Procedure. As code validation is required to evaluate the accuracy of the computational procedure of a problem, we have accomplished comparisons considering mixed convection in different configurations:

3.5.1. Validation Case One. Rashad et al. [60] simulated mixed convection in a lid-driven cavity filled with nanofluids by implementing the finite volume method and compared their results with earlier studies reported by Khanafer and Chamkha [61] and Iwatsu et al. [62]. We have simulated the similar studies of those [60–62] by using a finite element method-based numerical code. The obtained results are compared with their results and presented in Table 4. In

addition, comparative results of isotherm plotting are also presented in Figure 5(a). In both cases, numerically and graphically, rational agreements are found.

3.5.2. Validation Case Two. Du et al. [63] used the finite difference method to investigate the influence of a magnetic field on open cavity flow and validated their numerical code with numerical results available in [50, 64]. They also validated their numerical code by comparing stream function and temperature contours against the stream function and temperature contours reported by Ghasemi et al. at [50]. In this study, we have implemented our numerical procedure to solve the problems relating to [50, 63, 64] in special cases, and the obtained results are validated by performing comparisons as shown in Table 5 and Figure 5(b).

Thus, the above comparisons ensure that the present numerical procedure is suitable to simulate mixed convection in a nanofluid-filled square domain equipped with baffles and a rotating hollow cylinder having roughness components and also an external magnetic field which leads us to carry on our investigation.

4. Results and Discussion

In this section, simulated results are obtained for mixed convection of Al_2O_3 -water nanofluid in a lid-driven cavity with horizontal baffles and a cantered rotating rough cylinder, and the flow and thermal fields are demonstrated using physical quantities streamlines, temperature contours, and average Nusselt number bar charts consistently. During simulation and graphic presentation, variation in two parameters is considered simultaneously while the values of others are kept fixed as $\text{Pr} = 6.2$, $\text{Gr} = 100$, $\text{Sr} = 10$, $\text{Ha} = 10$, $\text{Re} = 100$, $\phi = 1\%$, $\text{Bh} = 0.20 \text{ L}$, and $\Delta = 0.0275 \text{ L}$. As a result, the sole effects of the two governing parameters have been exhibited combinedly. The parametric ranges of the analysis are presented in Table 6.

4.1. Effects of Speed Ratio (Sr) and Magnetic Field (Ha) on Streamlines. Figure 6 illustrates the flow field by plotting streamlines for different values of the speed ratio of the rotating rough cylinder and magnetic field strength in the presence of mounted horizontal baffles. In Figure 6(a) at motionless state of the rough cylinder and $\text{Ha} = 0$, heated-fluid ascends near the left vertical wall due to thermal induced-buoyancy flow and then descends quickly from top to bottom near the right vertical walls as the top moving cold wall and insulated vertical wall flow circulates in downward direction. As a result, clockwise streamline circulation is developed within the cavity, which is also confirmed by the negative flow strength. This convective circulation occupies the whole cavity, and it is found suppressing by the presence of horizontal baffles. Moreover, the highest flow strength is noticed at -0.065 within the core circulation near the top

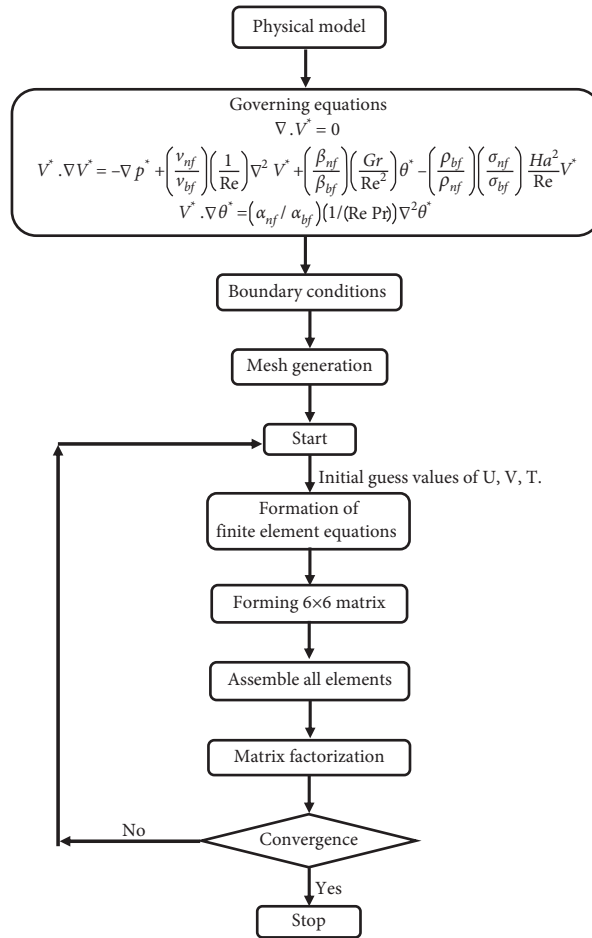


FIGURE 2: Flowchart of the FEM.

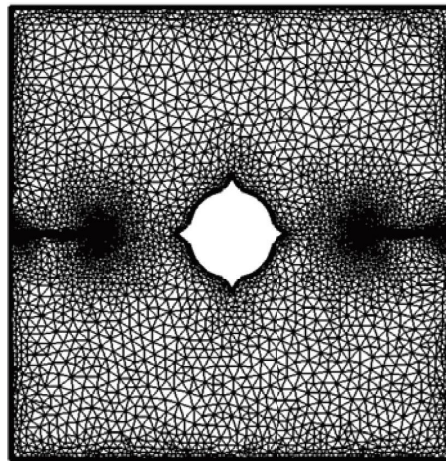


FIGURE 3: Mesh generation of the square cavity.

TABLE 3: Average Nusselt number at different mesh systems.

Nodes (elements)	8527 (16526)	13125 (25482)	17342 (33712)	24444 (47648)	32702 (63999)
Nu_{av}	9.439	9.521	9.581	9.607	9.618

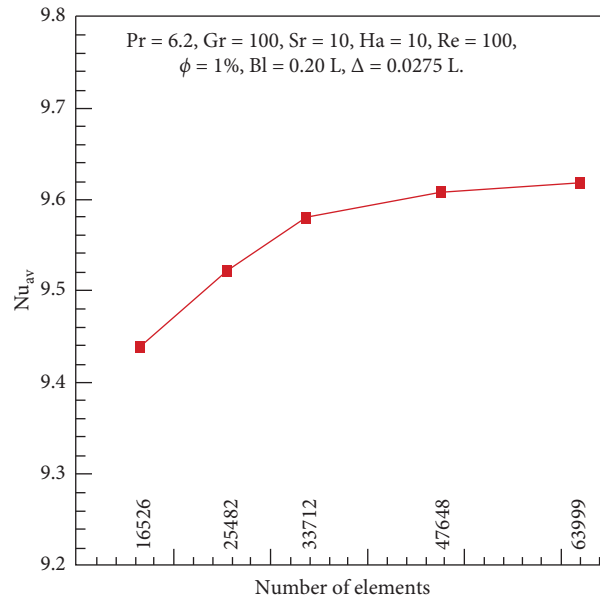


FIGURE 4: Grid refinement test.

TABLE 4: Comparison of calculated Nu_{av} at $Pr = 0.71$ and $Gr = 10^2$.

Re	Iwatsu et al. [62]	Khanafar and Chamkha [61]	Rashad et al. [60]	Present study	Dev (%) [61]
100	1.94	2.01	1.93	2.02	0.49
400	3.84	3.91	3.91	3.94	0.77
1000	6.33	6.33	6.31	6.39	0.95

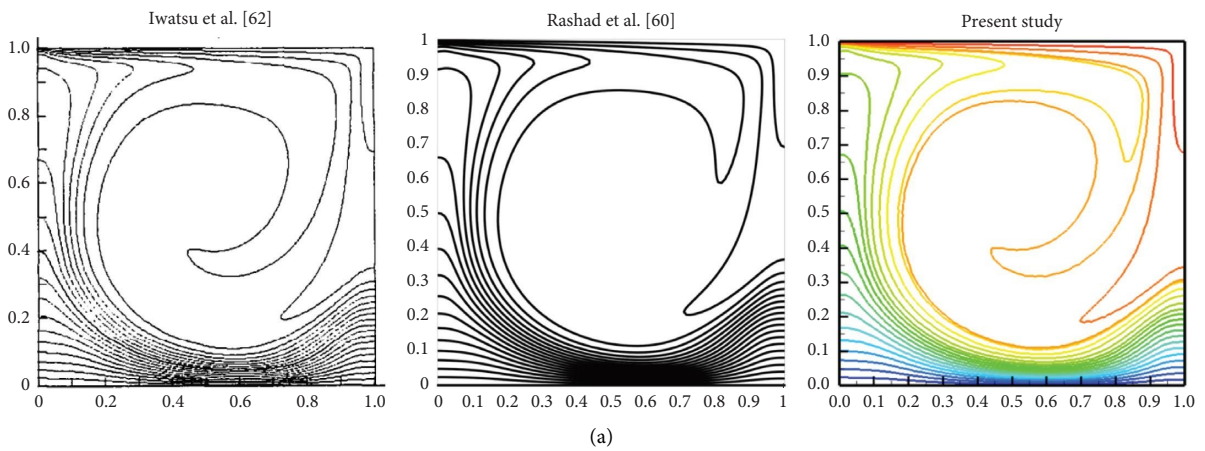


FIGURE 5: Continued.

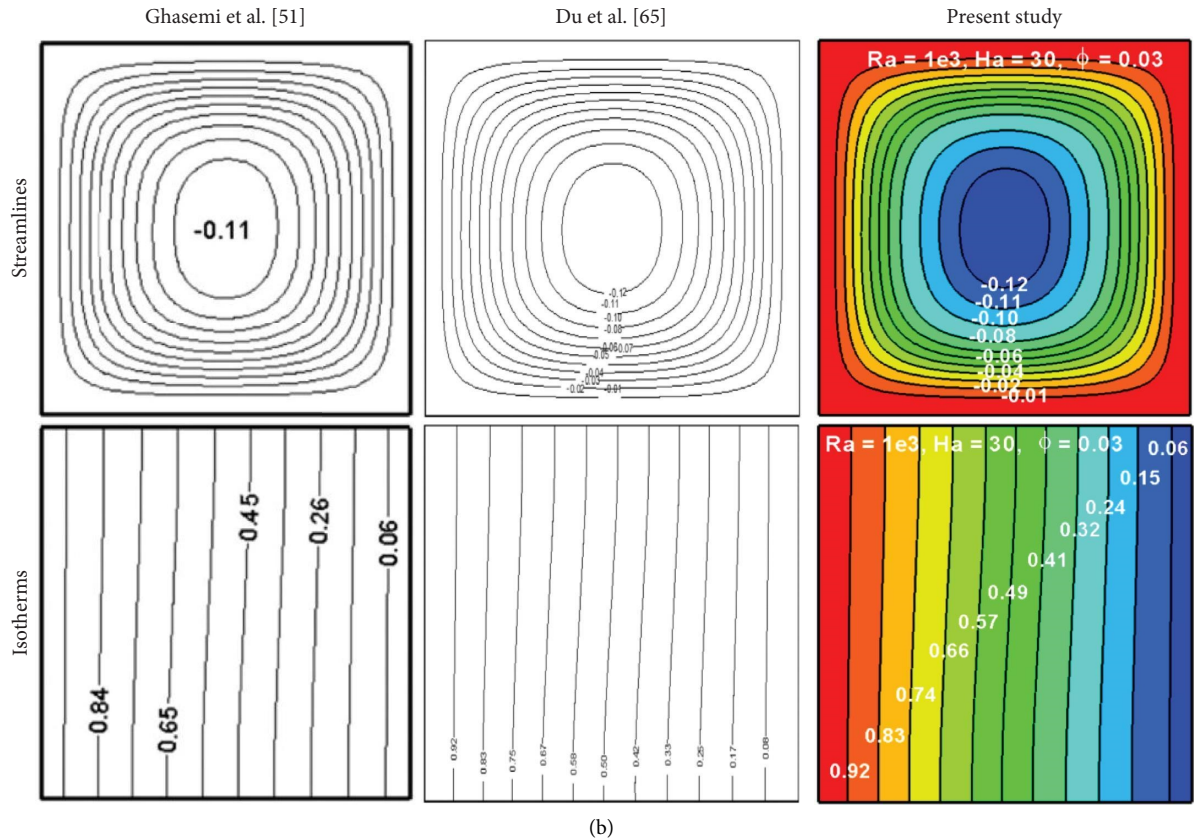


FIGURE 5: (a) Comparison of temperature contours for the present study against the earlier studies [59, 61]. (b) Comparison of streamline and isotherm plotting.

TABLE 5: Comparison of average Nusselt number.

	$Ha = 0$		$Ha = 30$	
	$\phi = 0$	$\phi = 0.02$	$\phi = 0$	$\phi = 0.02$
Ghasemi et al. [50]	4.738	4.820	3.150	3.138
Pordanjani et al. [64]	4.654	4.813	3.147	3.143
Du et al. [63]	4.746	4.837	3.169	3.238
Present study	4.736	4.819	3.149	3.221
Dev (%) [63]	0.2111	0.498	0.635	0.527

TABLE 6: Parametric ranges.

Sr: Ha	0–20 : 0–50
Re: Ha	10–200 : 0–50
ϕ : Ha	0%–5% : 0–50
Δ : Ha	0.0000 L–0.0375 L : 0–50
Bl: Ha	0.10 L–0.25 L : 0–50
Baffles orientation: Ha	Baffles positions: 0–50

moving wall. After that, rough cylinder gets rotating at speed $Sr = 5$, the flow circulation is restructured by compressing the clockwise-circulations toward the top wall and forming anticlockwise circulation around the rough cylinder with the influence of rotating inertia of rough cylinder. It is also found that flow velocity increased rapidly, and the strength as well as intensification of flow circulations around the hollow cylinder is much stronger than those close to the top wall. Later on, when speed ratio increased to $Sr = 10$, more rotating inertia is produced within the cavity, and hence, the

effect of the moving wall is dominated. As a result, streamline circulation becomes more intensified with higher strength around the rotating obstacle. Further increase in rotating speed to $Sr = 20$, the anticlockwise circulation gets maximum size and strength, whereas the clockwise circulation becomes small and close to the top wall. In order to visualize the impact of the speed of the rotating rough cylinder, we have recorded the numerical flow velocities and these are 0.065 at $Sr = 0$, 0.060 at $Sr = 5$, 1.10 at $Sr = 10$, and 2.40 at $Sr = 20$. In all diagrams, streamline circulations are found squeezing from its both sides due to the presence of adiabatic baffles, as a result flow circulation is retarded by the baffles and gets lower strength. On the other hand, mixed convection circulations are remained almost similar for varying rotating speed while magnetic field is imposed at strength $Ha = 10$ compared to the earlier case ($Ha = 0$), but its strength decreases remarkably. Further increase in

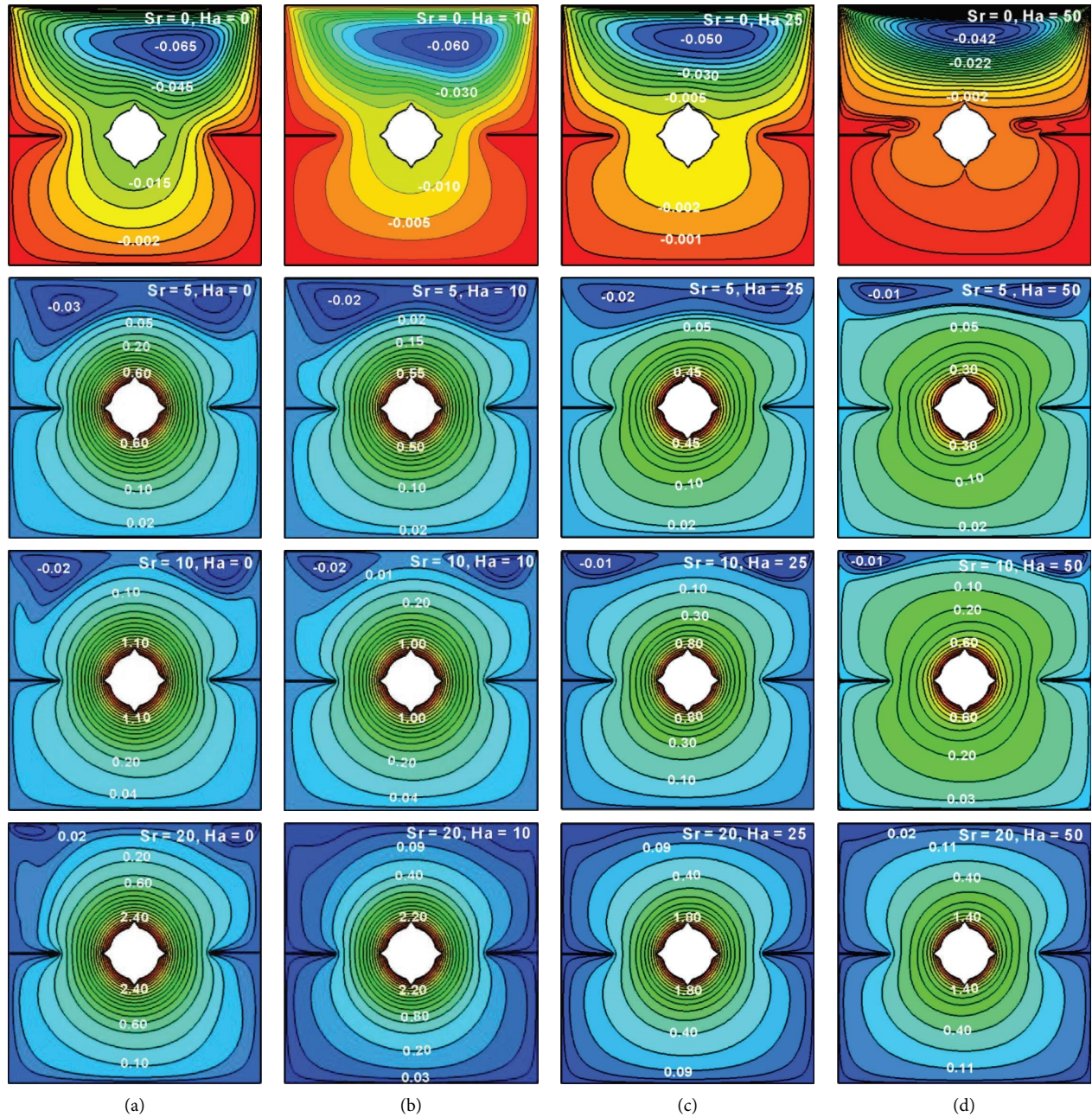


FIGURE 6: Variation in streamline plotting for different Sr and Ha.

Ha = 25, streamlines are spaced out with lower strength compared to the case at Ha = 10. In addition, streamlines are more affected and spaced out at Ha = 50 and also gets minimum strength. The physical consequences behind it is the Lorentz's force retards flow velocity which is produced due to the interaction of nanofluid buoyancy flow and shear flow with an imposed magnetic force, and the Lorentz's force escalates with each increment in the magnetic effect. As a result, flow circulation declines with an increase in Ha for all Ra. Thus, one can conclude that the variation in flow characteristics is more noticeable at greater magnetic field strengths than at lower ones, while compared in the absence of a magnetic field.

4.2. *Effects of Speed Ratio (Sr) and Magnetic Field (Ha) on Isotherms.* Figure 7 represents the thermal field via temperature contour plotting as well as its topology due to combined variation in rotational speed of rough cylinder and magnetic field strength at fixed values of other parameters such as Pr = 6.2, Re = 100, Gr = 100, and $\phi = 1\%$. In Figure 7(a), at Sr = 0 and Ha = 0, isotherms are densely visible over the heated wall and then shifted in an upward direction near the left vertical wall resulting in an imposed thermal condition and clockwise flow circulation due to the top moving wall. In the case of a rotating rough cylinder at Sr = 5 (in a counter-clockwise direction), isotherms are reshuffled by forming a spinning shape around the rough

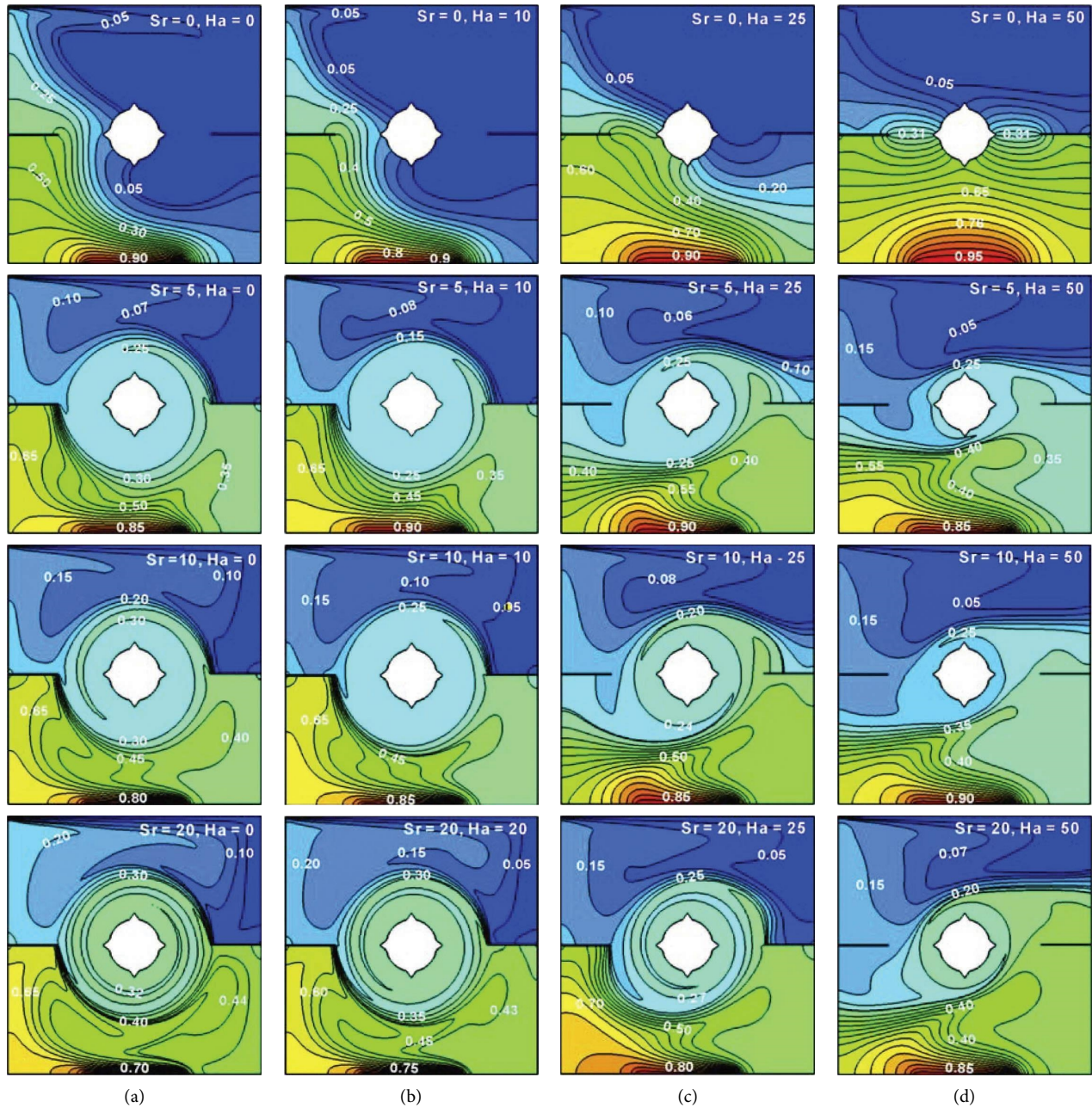


FIGURE 7: Variation in temperature contour plotting for different Sr and Ha .

cylinder that occupies a fluid domain inside the cavity. Moreover, isotherms close to the cold moving wall are found twisting in the direction of lid-wall motion. In all diagrams, especially while the rough cylinder is in motion, isotherm distribution is found reforming with the presence of baffles where the lower isotherm pack seems to be connected to the lower end of the left adiabatic baffle and another isotherm pack seems to initiate from the top end of the right adiabatic baffle and then complete isotherm circulation in the core region. It is worth noting that cylinder rotating -inertia dominates the lid force from the core region to the bottom region, and hence isotherms tend to spin in the direction of the rough cylinder. With each subsequent increment in rotation speed, isothermal distribution within the cavity is

significantly affected, core circulation becomes much stronger, and the isothermal pack near the bottom region is also more condensed toward the heated wall. As a result, more convective heat is released from the heated wall for each increment in the rotational speed of the rough cylinder. When the magnetic field is imposed at strength $Ha = 10$, small changes are noticed in temperature contour distribution for different speed ratios, but for $Ha = 25$ remarkable changes are recorded in the isotherms distribution for all Sr , especially in the core distribution of temperature contours. Further increment in magnetic field strength at $Ha = 50$, significant changes are observed in isotherm distributions within the closed domain which reflects the magnetic field has a significant impact on the distribution of isotherms as

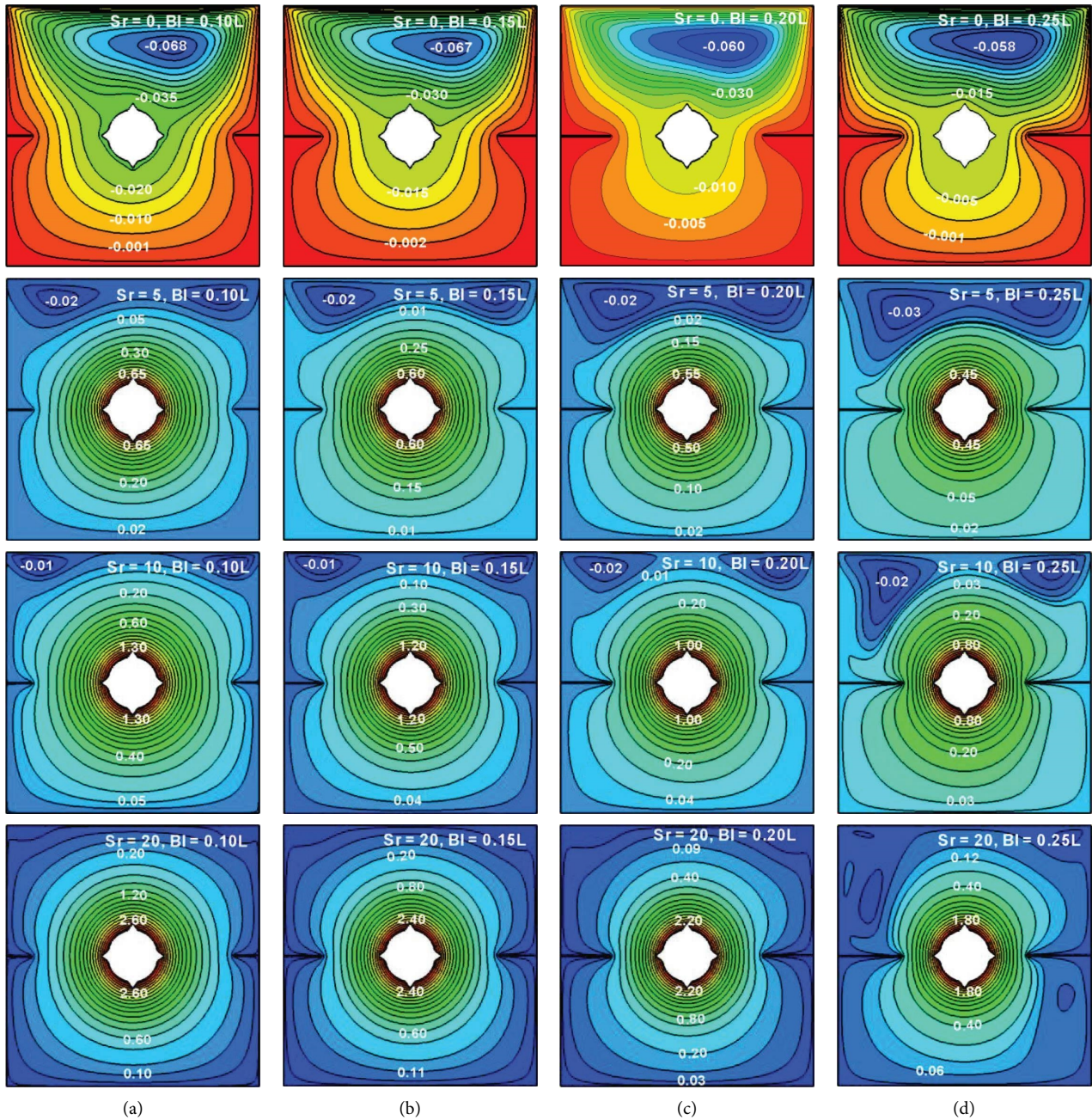


FIGURE 8: Variation in streamline plotting for different Sr and Bl.

well as temperature zones inside the cavity. Moreover, temperature plotting is found different for both increasing speed of rotation and strength of magnetic fields. Consequently, convective heat transferring reduces with Ha . In addition, different colours of temperature zones in the fluid domain indicate the topologies of the thermal field for varying amounts of Sr and Ha , respectively.

4.3. Effects of Speed Ratio (Sr) and Baffles Length (Bl) on Streamlines. The streamline plotting in nanofluid flow circulation at different speed ratios of rotating rough cylinder and baffles length is presented in Figure 8. In all

diagrams, streamline circulations are found squeezing by the baffles and it increases with the increase in length of both baffles. As a result, flowing nanofluid encounters more resistive force for longer baffles, and hence the strength of flow circulation is reduced noticeably. Moreover, the streamline pattern of core circulations is unchanged except in the regions where the baffles are horizontally located. In addition, secondary circulations over the core circulation are also more affected by the increased length of baffles. Thus, longer baffles cause more changes in the flow velocity as well as circulations compared to shorter baffles. Moreover, impact of baffles on the flow field is more effective while rough cylinder is rotated at highest speed ratio than lower as

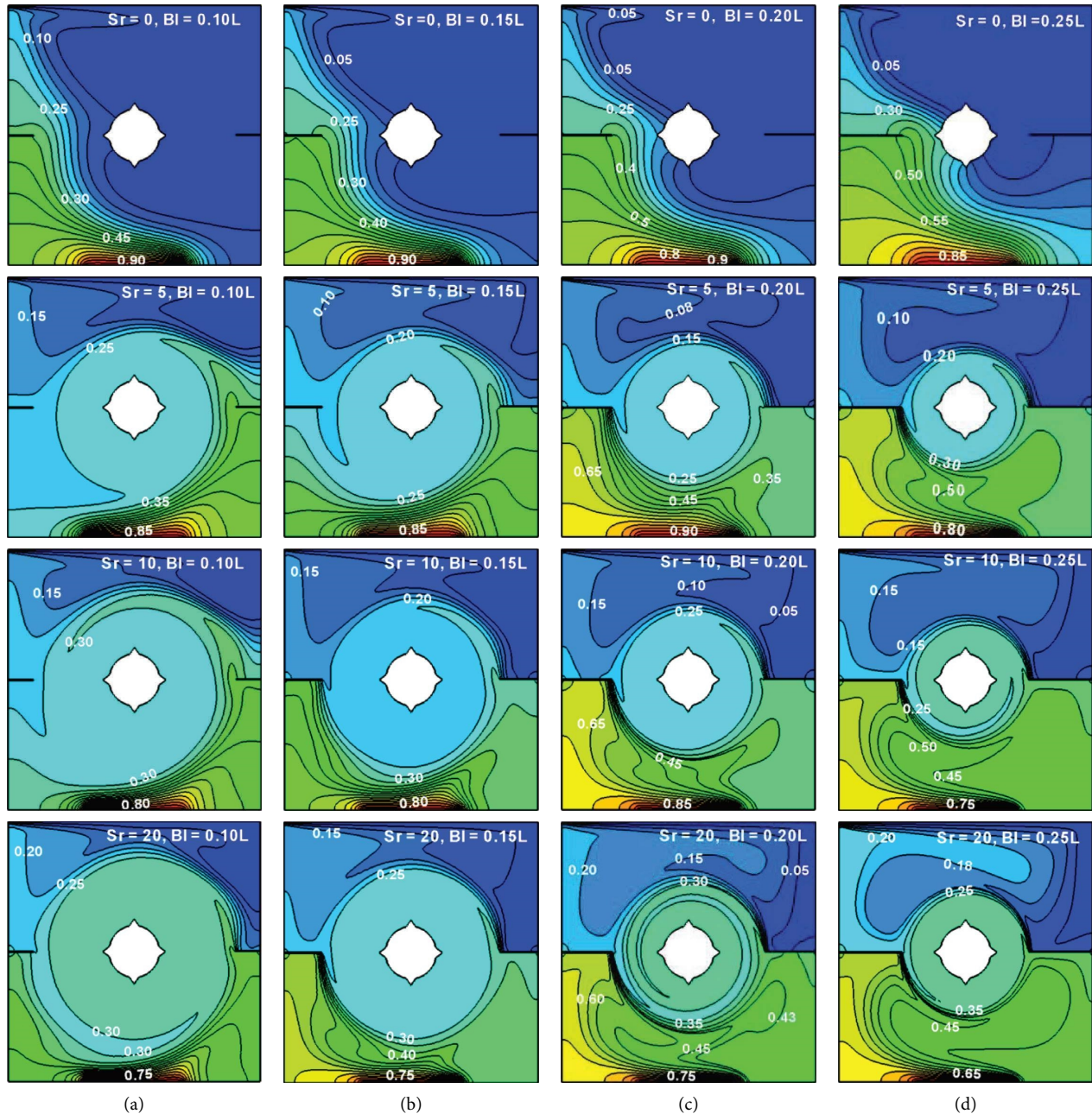


FIGURE 9: Variation in temperature contour plotting for different Sr and Bl.

44.44% reduction is found in flow strength at $Sr=20$ that becomes 17.24% at $Sr=0$.

4.4. Effects of Speed Ratio (Sr) and Baffles Length (Bl) on Isotherms. Besides this, Figure 9 displays isotherms of distribution when speed ratio and baffle length are increased simultaneously. The distribution of temperature contours is found and changes gradually especially in the core region, with the increase in length of baffles and denseness of isotherms, are also found getting closer to the bottom heated wall which results in heat transferring increase with longer baffles. It is required to note that the impact of baffle length on the thermal field decreases while the speed ratio gets

lower strength and it seems to be insignificant in the motionless state of the rough cylinder.

4.5. Effects of Reynolds Number (Re) and Magnetic Field (Ha) on Streamlines. The plotting of streamlines due to combined variation in Reynolds and Hartmann numbers is demonstrated in Figure 10. In Figures 10(a)–10(d), strong convective counter-clockwise flow circulations are observed around the rough cylinder due to the influence of cylinder rotating-inertia and the imposed thermal condition. In addition, two symmetric clockwise flow circulations are also visualized over the centred anticlockwise circulation with the assistance of

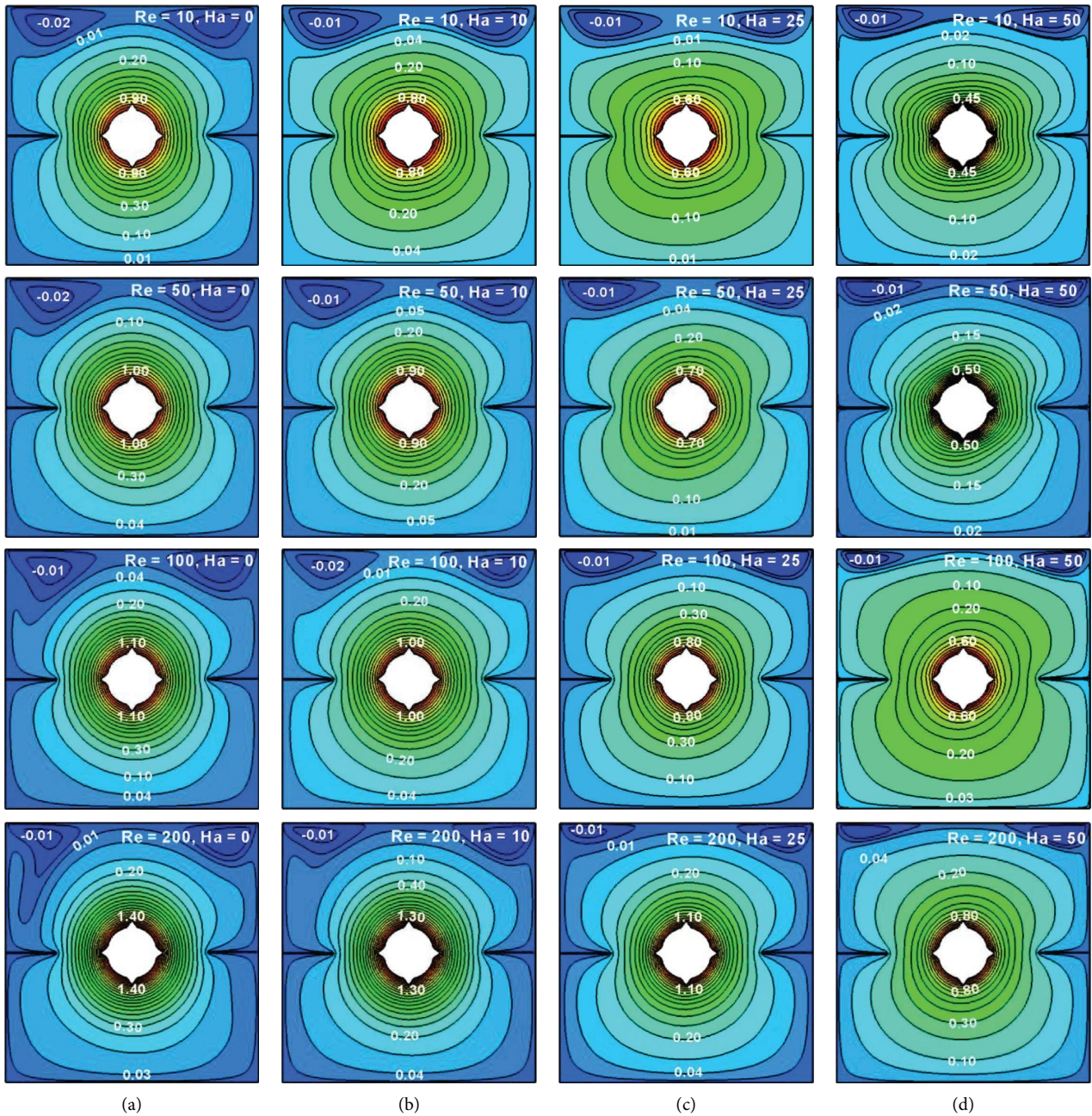


FIGURE 10: Variation in streamline plotting for different Re and Ha.

lid-wall inertia. However, the strength of convective flow circulations is observed increasing with the increase in Reynolds numbers and streamlines are also intensified toward the cylinder because increase in Re causes increment in fluid inertia which results rotating inertia and lid inertia are both increased, and hence strength as well as concentration of streamlines increased but the pattern of streamlines remained similar for varying Re. Besides this, it is noticed that the flow velocity gets lower strength, and distribution of streamlines is spaced out toward the boundaries with an increasing Ha for all Re. These variations are more noticeable in higher magnetic strength than comparative lower ones.

4.6. *Effects of Reynolds Number (Re) and Magnetic Field (Ha) on Isotherms.* On the other hand, isotherm distributions at different Re and Ha are depicted in Figure 11. It is observed that isotherms are generated from the heated wall and distorted around the rough cylinder covering the fluid domain due to the rotating rough cylinder and moving wall in the presence of baffles. As lower Re causes lower fluid inertia, rotating inertia and lid inertia lose their inertia at $Re = 10$, and hence a weak isotherm circulation is visible around the cylinder and isotherms become wavy with lower gradient near the top wall (as seen in Figure 11(a) at $Ha = 0$). As a result, lower heat transfer occurs at $Re = 10$. After that,

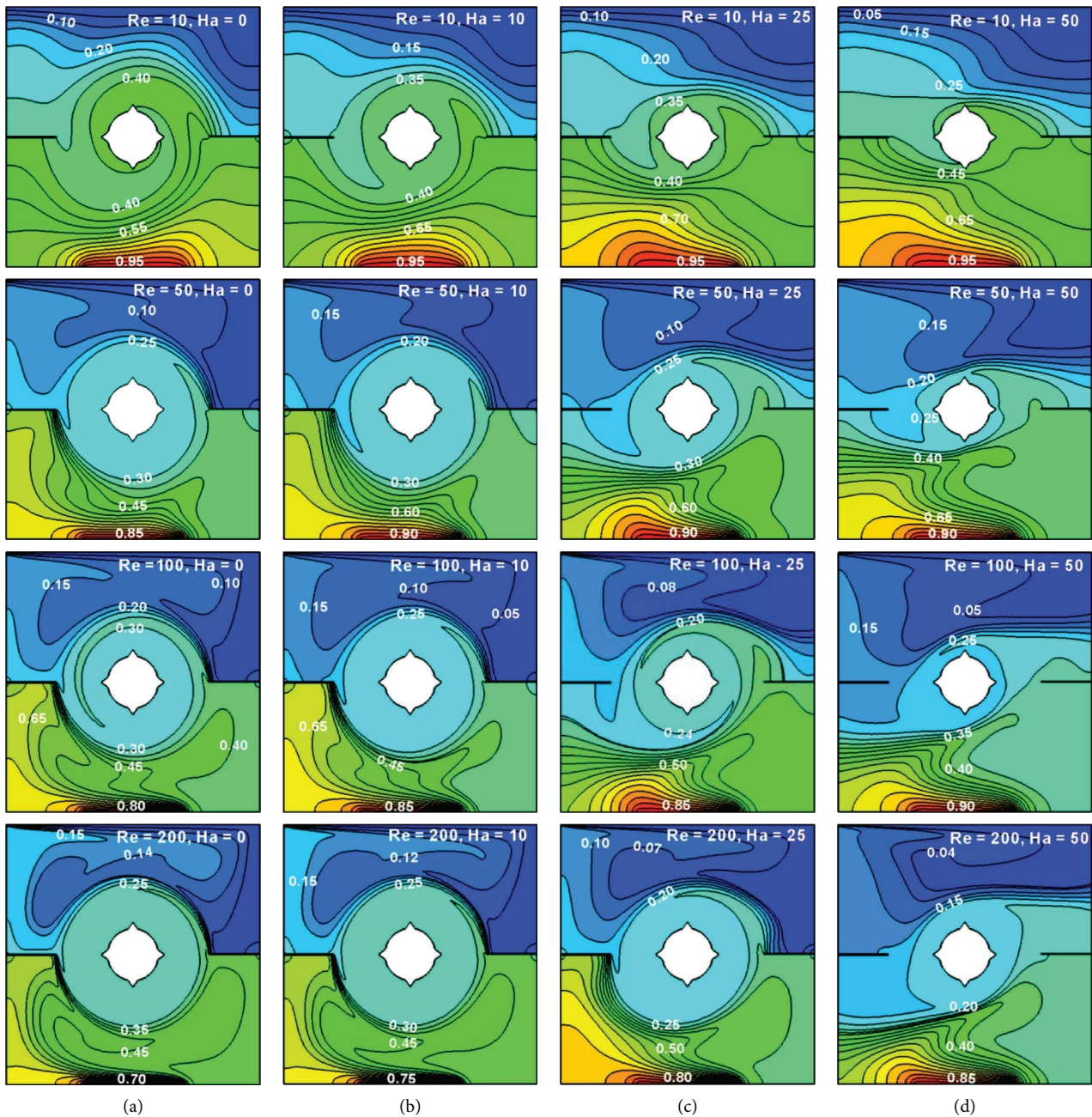


FIGURE 11: Variation in temperature contour plotting for different Re and Ha.

increasing Re increase fluid inertia consequently, both rotating inertia and lid inertia become prominent, and hence isotherms circulation around the cylinder become stronger and isotherms are more twisted near the top moving wall up to $Re = 100$. Then at $Re = 200$, circulation and distortion of isotherms become more stronger having higher thermal gradient which results more convective heat released at $Re = 200$. When magnetic field is imposed at $Ha = 10$, isotherms distribution slightly changed for all Re. Further increase in Ha, circulation, and distortion of isotherms remarkably get affected, and the effect of Ha is found prominent at lower Re than at higher Re. Moreover, dense circulation rounding the rough cylinder tends to disappear,

and isotherms are spaced out with a lower curvature at $Ha = 50$, which confirms the substantial effect of the magnetic field on isotherm distribution for all Re.

4.7. Effects of Volume Fraction (ϕ) and Magnetic Field (Ha) on Streamlines. Figure 12 delineates streamlines plotting for different volume fractions of nanoparticles in a lid-driven cavity having a rotating cylinder with triangular components in the presence of a magnetic field or not. Due to induced thermal and velocity boundary conditions, a primary convective strong flow circulations along with two secondary small circulation are visible in the base fluid at fixed parametric values as $Pr = 6.2$, $Gr = 100$, $Sr = 10$, $Re = 100$,

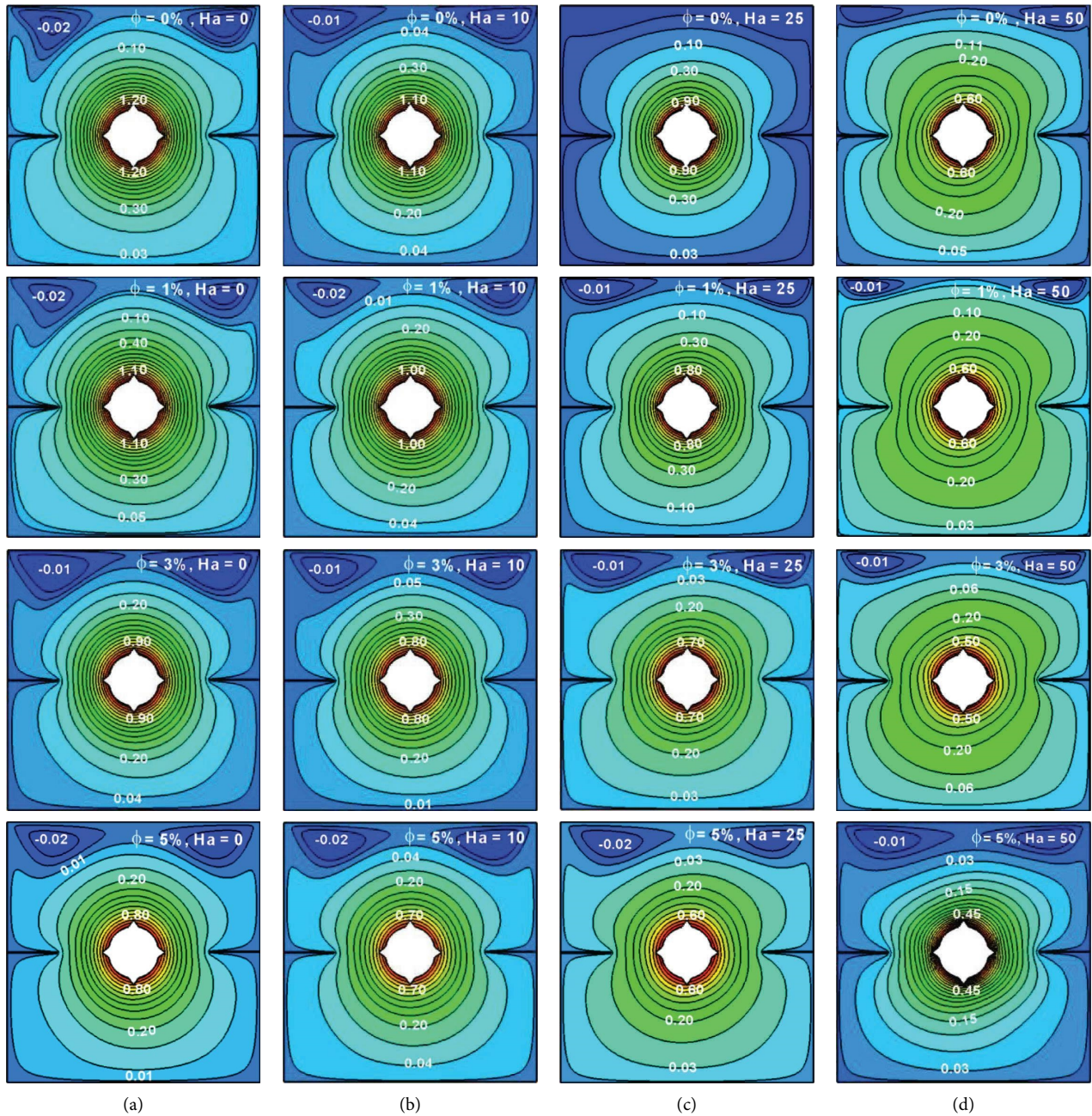


FIGURE 12: Variation in streamline plotting for different ϕ and Ha .

$Bh = 0.20 L$, and $\Delta = 0.0275 L$, which remain almost similar in nanofluids at different concentrations (1%, 3%, and 5%), but flow strength is found declining remarkably for the additional nanoparticles at vol. of 1%, 3%, and 5% in the base fluid. These results are expected since the amalgamation of nanoparticles increases the density of the working fluid and decelerates flow velocity within the cavity. In order to understand the flow magnitude at different amounts of nanoparticles more accurately, one can find the maximum velocity at the core flow circulations which are 1.20, 1.10, 0.90, and 0.80, respectively, at vol. of 1%, 3%, and 5%. It is also found that flow velocity decreases for imposing and increasing magnetic field strength transverse to the flow

circulation. Moreover, denseness of streamlines reduces with each increment in Ha and spaced out toward the sidewalls. In addition, maximum declination in flow magnitude id occurred at simultaneous changes in the volume fraction and magnetic field which are recorded as 1.2 ($\phi = 0\%$, $Ha = 0$), 1.0 ($\phi = 1\%$, $Ha = 10$), 0.70 ($\phi = 3\%$, $Ha = 25$), and 0.45 ($\phi = 5\%$, $Ha = 50$).

4.8. Effect of Volume Fraction (ϕ) and Magnetic Field (Ha) on Isotherms. Beside these, distributions of temperature contours in base fluid and nanofluid with 1% volume fraction are found (in Figure 13(a)) qualitatively similar but minute

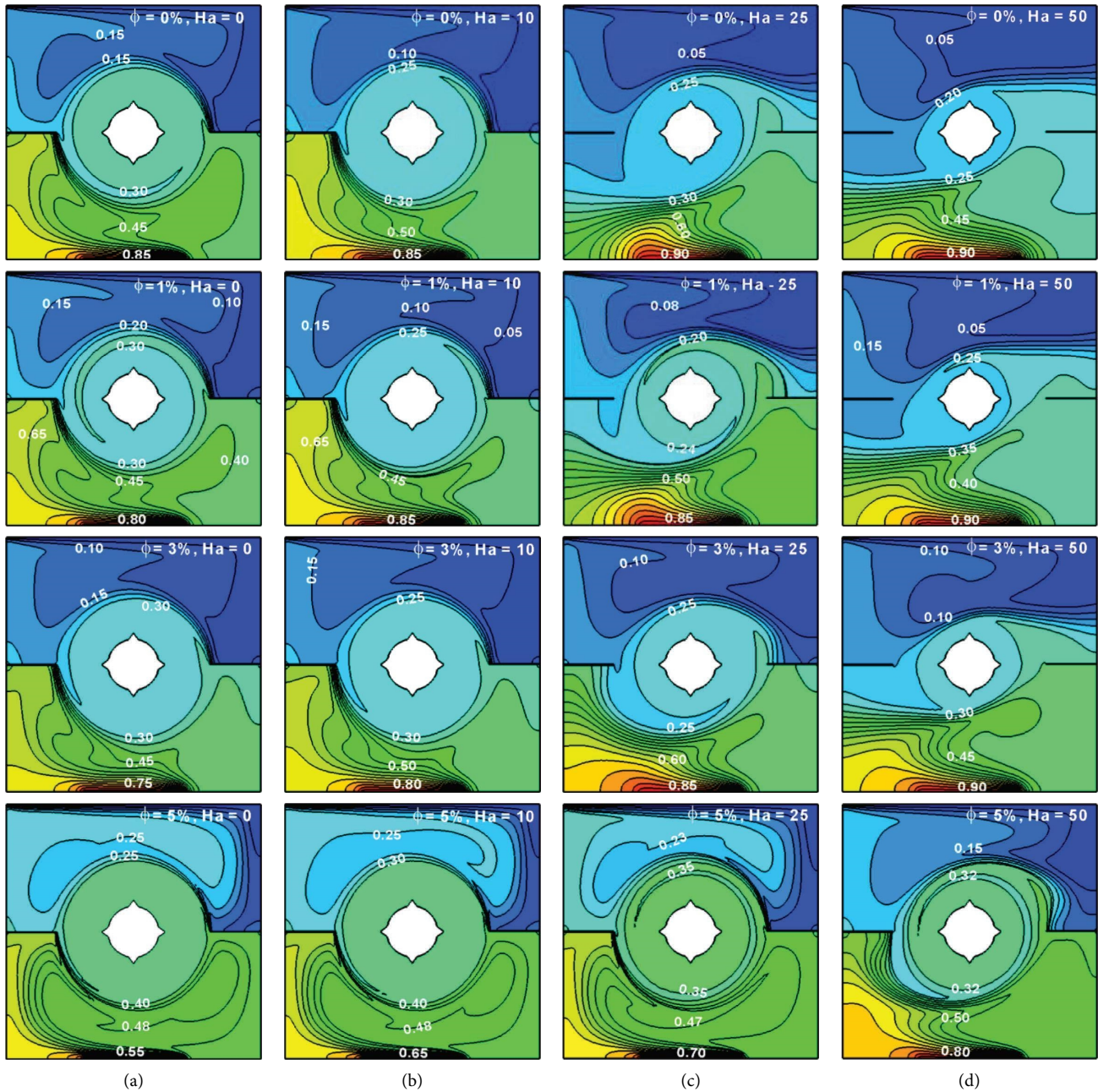


FIGURE 13: Variation in temperature contour plotting for different ϕ and Ha .

changes are noticed for vol. of 3% and 5%. The physical reason behind is that the presence of nanoparticles in base fluid decreases convection mode and hence increases the domination of conduction mode heat transfer. It is necessary to note that isotherms distributions substantially change in both base fluid and nanofluid at highest magnetic field strength compared to at lowest.

4.9. Effect of Ha along with Sr , Re , ϕ , Δ , Bl , and Baffles Orientations on Average Nusselt Number (Nu_{av}). Figure 14 illustrates heat transferring in the fluid flow domain due to physical parameters via average Nusselt number bar charts. Figure 14(a) confirms the heat transfer rate augments rapidly

with increasing rotational speed of rough cylinder because increased rotational inertia due to Sr increases flow circulation significantly. It is also visualized in Figure 14(a) that higher magnetic strength decreases the heat transfer rate at each Sr as the interaction of magnetic force with convective flow circulation generates Lorentz's force, which reduces the flow velocity and produces more temperature within the fluid domain. From Figure 14(b), it is seen that the heat transfer rate augments monotonically by the increasing Re where maximum heat transfer is recorded in forced convection dominated regime and minimum for mixed convection regime. The physics behinds it is that higher Re increases fluid inertia which accelerates cylinder rotating inertia and also lid inertia that causes maximum flow circulation and heat transfer within the cavity.

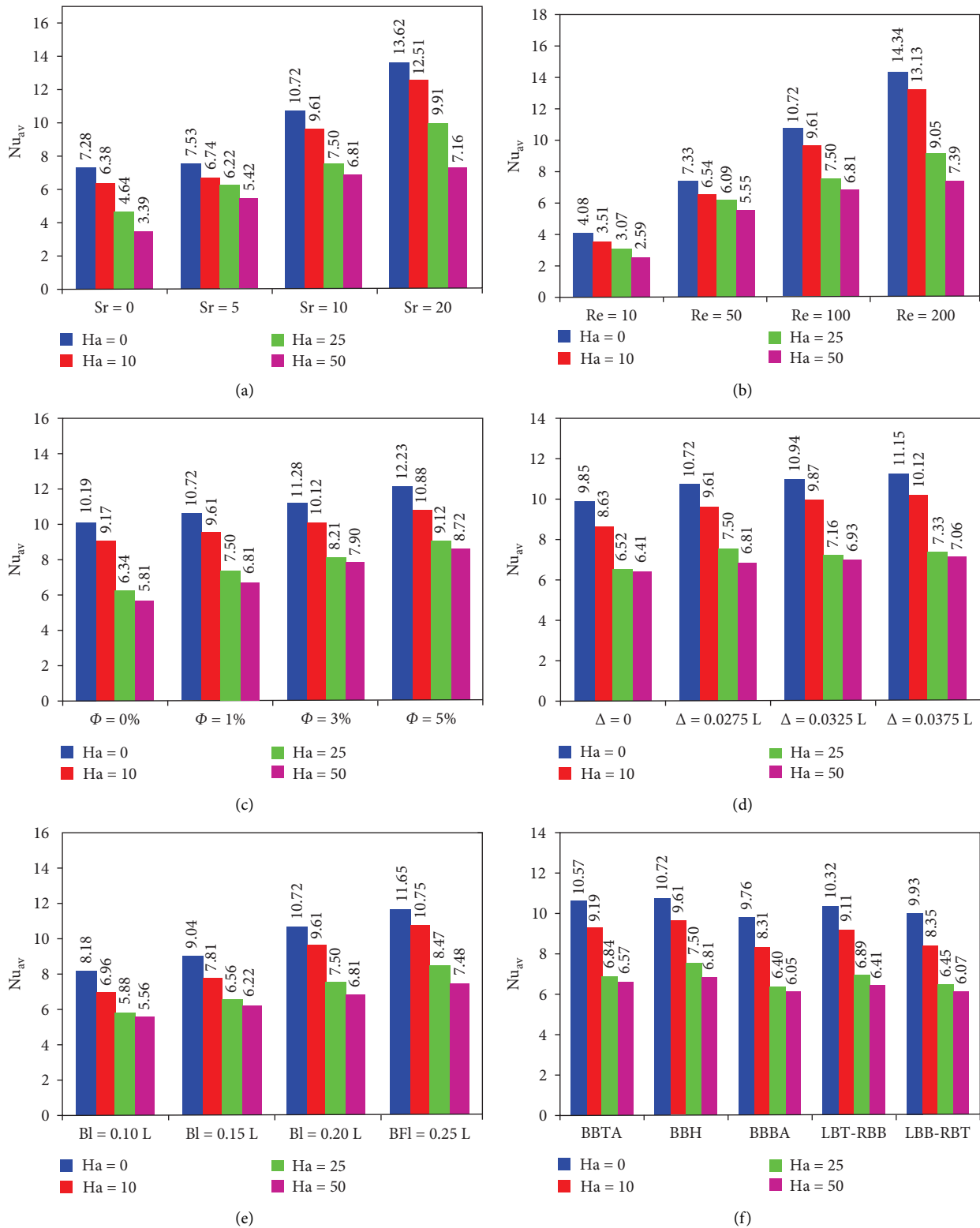


FIGURE 14: Variation in average Nusselt for different Sr , Ha , Re , ϕ , Δ , Bl , and orientation of baffles.

In Figure 14(c), the heat transfer rate is found increasing the function of the amount of nanoparticles. This phenomenon is expected as higher amounts of nanoparticles improves nanofluid thermal conductivity, and hence capability of energy transportation in the flow domain. A similar trend is also

observed in Figure 14(d) for the presence and increase in height of triangular components on the rotating cylinder, as higher heights of triangular components increase rotating inertia and flow velocity as well. In order to understand the impact of roughness components on heat transferring precisely, it

can be recorded that 13.20% (at $Ha = 0$) more heat transfer takes place for rotating rough cylinders compared to rotating smooth cylinders, and it becomes 10.14%, while the magnetic field is activated at strength $Ha = 50$. On the other hand, enhancement in heat transfer is found for enlarging baffles length (seen in Figure 14(e)) as the temperature contours were found getting closer to the heated wall with longer baffles and also concentrated in its distribution around the rough cylinder, which leads to an increase in heat transferring inside the cavity (shown in Figure 9). Moreover, heat transfer rate increases by 42.42% while baffle length changes from $0.10L$ to $0.25L$ in the absence of a magnetic field but reduces to 34.53% while the magnetic field is activated at a strength of $Ha = 50$. Results in Figure 14(f) indicate that the average Nusselt number strongly depends on the orientation of baffles, and maximum heat transfer occurs while baffles are horizontally fixed at the cavity's vertical walls. In all bar charts of Nusselt number, it is observed that the heat transfer rate decelerates monotonically with the increase in magnetic field strength resulting in active Lorentz's force due to the magnetic field effect.

5. Conclusions

In this study, the impacts of the magnetic field, rotating rough cylinder, and amount of nanoparticles on the fully developed flow and temperature fields in a nanofluid filled, partially heated lid driven cavity with horizontal baffles are numerically investigated. The Galerkin finite element method is implemented to simulate the governing equations, and the obtained results are validated against existing results available in the literature. Detailed parametric discussion has been performed based on the physical point of view. The major findings based on the obtained results are as follows:

- (i) Intense streamline circulation and fluid flow velocity are occurred at higher speed ratios and Reynolds number, while the reverse phenomenon is occurred at higher magnetic field strengths, nanoparticle concentrations, and length of the baffles.
- (ii) The temperature contour plotting changes significantly with the change in speed of rotating rough cylinder, Reynolds and Hartmann numbers, and baffles length, while rough cylinder is in motion but it minutely changes with the increase in concentration of nanoparticles in the base fluid.
- (iii) Heat transfer rate is augmented substantially at higher speed ratio, height of the triangular components, length of baffles, and Reynolds number, which is respectively maximized and minimized at each increment in nanoparticle volume fraction and magnetic field strength.
- (iv) heat transfer rate is optimum, while baffles are horizontally fixed at the cavity walls than other cases.

- (v) Maximum heat transfer occurred while triangular components are attached to the rotating cylinder rather than a smooth rotating cylinder.
- (vi) Optimization of heat transfer is correlated with the direction of rotating the rough cylinder and lid wall.

Nomenclature

\vec{B} :	External magnetic field vector
B_0 :	Magnetic field strength ($W b m^{-2}$)
Bl :	Baffles length (m)
d_{np} :	Nanoparticle diameter (nm)
c_p :	Specific heat at constant pressure ($J kg^{-1} K^{-1}$)
\vec{g} :	Gravitational acceleration vector
g :	Gravitational acceleration ($m s^{-2}$)
Gr :	Grashof number ($g \beta_{bf} (T_h - T_c) L^3 / \nu_{bf}^2$)
Ha :	Hartmann number ($B_0 L \sqrt{\sigma_{bf} / \mu_{bf}}$)
I :	Electric current vector
L :	Length of the cavity (m)
k :	Thermal conductivity ($W m^{-1} K^{-1}$)
n :	Unit vector normal to walls
Pr :	Prandtl number (ν_{bf} / α_{bf})
p^* :	Dimensionless pressure
R :	Radius of the cylinder (m)
Re :	Reynolds number ($U_0 L / \nu_{bf}$)
T :	Dimensional temperature (K)
V^* :	Dimensionless velocity vector components
U_0 :	Lid velocity ($m s^{-1}$)
x, y :	Dimensional coordinates (m)
x^*, y^* :	Dimensionless coordinates

Greek symbols

α :	Fluid thermal diffusivity ($m^2 s^{-1}$)
β :	Thermal expansion coefficient (K^{-1})
θ^* :	Dimensionless
μ :	Dynamic viscosity ($N s m^{-2}$)
ν :	Kinematic viscosity ($m^2 s^{-1}$)
ν :	Kinematic viscosity ($m^2 s^{-1}$)
ρ :	Density ($kg m^{-3}$)
σ :	Electrical conductivity ($S m^{-1}$)
ϕ :	Volume fraction of nanoparticles
φ :	Electric potential
ω :	Nondimensional angular velocity of rotating rough cylinder

Symbols

Δ : Triangular components on the cylinder

Subscripts

bf :	Base fluid
h :	Hot
c :	Cold
nf :	Nanofluid
np :	Nanoparticles

Abbreviations

BBTA:	Both baffles top angulated
BBH:	Both baffles horizontal
BBBA:	Both baffles bottom angulated
LBT-RBB:	Left baffle top angulated-right baffle bottom angulated
LBB-RBT:	Left baffle bottom angulated-right baffle top angulated.

Data Availability

The data used to support the findings of this study can be obtained from the corresponding author upon request.

Conflicts of Interest

The authors declare that they have no conflicts of interest.

References

- [1] A. Fereidoon, S. Saedodin, M. Hemmat Esfe, and M. J. Noroozi, "Evaluation of mixed convection in inclined square lid-driven cavity filled with Al₂O₃/water nano-fluid," *Engineering Applications of Computational Fluid Mechanics*, vol. 7, no. 1, pp. 55–65, 2013.
- [2] M. Muthamilselvan and D. H. Doh, "Magnetic field effect on mixed convection in a lid-driven square cavity filled with nanofluids," *Journal of Mechanical Science and Technology*, vol. 28, no. 1, pp. 137–143, 2014.
- [3] M. A. Ismael, M. A. Mansour, A. J. Chamkha, and A. M. Rashad, "Mixed convection in a nanofluid filled-cavity with partial slip subjected to constant heat flux and inclined magnetic field," *Journal of Magnetism and Magnetic Materials*, vol. 416, pp. 25–36, 2016.
- [4] A. Kasaeipoor, B. Ghasemi, and S. M. Aminossadati, "Convection of Cu-water nanofluid in a vented T-shaped cavity in the presence of magnetic field," *International Journal of Thermal Sciences*, vol. 94, pp. 50–60, 2015.
- [5] G. H. R. Kefayati, "Mixed convection of non-Newtonian nanofluid in an enclosure using Buongiorno's mathematical model," *International Journal of Heat and Mass Transfer*, vol. 108, pp. 1481–1500, 2017.
- [6] H. F. Öztop, A. Sakhrieh, E. Abu-Nada, and K. Al-Salem, "Mixed convection of MHD flow in nanofluid filled and partially heated wavy walled lid-driven enclosure," *International Communications in Heat and Mass Transfer*, vol. 86, pp. 42–51, 2017.
- [7] T. Armaghani, A. Kasaeipoor, N. Alavi, and M. M. Rashidi, "Numerical investigation of water-alumina nanofluid natural convection heat transfer and entropy generation in a baffled L-shaped cavity," *Journal of Molecular Liquids*, vol. 223, pp. 243–251, 2016.
- [8] A. Karimdoost Yasuri, M. Izadi, and H. Hatami, "Numerical study of natural convection in a square enclosure filled by nanofluid with a baffle in the presence of magnetic field," *Iranian Journal of Chemistry and Chemical Engineering (International English Edition)*, vol. 38, no. 5, pp. 209–220, 2019.
- [9] A. K. Hussein, M. Ghodbane, Z. Said, and R. S. Ward, "The effect of the baffle length on the natural convection in an enclosure filled with different nanofluids," *Journal of Thermal Analysis and Calorimetry*, vol. 23, 2020.
- [10] A. Zaim, A. Aissa, F. Mebarek-Oudina et al., "Galerkin finite element analysis of magneto-hydrodynamic natural convection of Cu-water nanoliquid in a baffled U-shaped enclosure," *Propulsion and Power Research*, vol. 9, no. 4, pp. 383–393, 2020.
- [11] S. Aljabair, A. L. Ekaid, S. H. Ibrahim, and I. Alesbe, "Mixed convection in sinusoidal lid driven cavity with non-uniform temperature distribution on the wall utilizing nanofluid," *Heliyon*, vol. 7, no. 5, p. e06907, Article ID e06907, 2021.
- [12] K. Al-Farhany, K. K. Al-Chlahawi, M. F. Al-dawody, N. Biswas, and A. J. Chamkha, "Effects of fins on magneto-hydrodynamic conjugate natural convection in a nanofluid-saturated porous inclined enclosure," *International Communications in Heat and Mass Transfer*, vol. 126, p. 105413, Article ID 105413, 2021.
- [13] I. A. Shah, S. Bilal, A. Akgül et al., "On analysis of magnetized viscous fluid flow in permeable channel with single wall carbon nano tubes dispersion by executing nano-layer approach," *Alexandria Engineering Journal*, vol. 61, no. 12, pp. 11737–11751, 2022.
- [14] S. Bilal, M. Rehman, S. Noeiaghdam, H. Ahmad, and A. Akgül, "Numerical analysis of natural convection driven flow of a non-Newtonian power-law fluid in a Trapezoidal enclosure with a U-shaped constructal," *Energies*, vol. 14, no. 17, p. 5355, 2021.
- [15] S. Bilal, N. Z. Khan, I. A. Shah, J. Awrejcewicz, A. Akgül, and M. B. Riaz, "Numerical study of natural convection of power law fluid in a square cavity fitted with a uniformly heated T-fin," *Mathematics*, vol. 10, no. 3, p. 342, 2022.
- [16] I. A. Shah, S. Bilal, A. Akgül, M. Omri, J. Bouslimi, and N. Z. Khan, "Significance of cold cylinder in heat control in power law fluid enclosed in isosceles triangular cavity generated by natural convection: a computational approach," *Alexandria Engineering Journal*, vol. 61, no. 9, pp. 7277–7290, 2022.
- [17] S. Bilal, I. A. Shah, M. Ramzan et al., "Significance of induced hybridized metallic and non-metallic nanoparticles in single-phase nano liquid flow between permeable disks by analyzing shape factor," *Scientific Reports*, vol. 12, no. 1, pp. 3342–3357, 2022.
- [18] M. Z. A. Qureshi, S. Bilal, M. B. Ameen, T. Mushtaq, and M. Y. Malik, "Numerical examination about entropy generation in magnetically effected hybridized nanofluid flow between orthogonal coaxial porous disks with radiation aspects," *Surfaces and Interfaces*, vol. 26, p. 101340, Article ID 101340, 2021.
- [19] Z. A. Qureshi, S. Bilal, I. A. Shah et al., "Computational analysis of the morphological aspects of triadic hybridized magnetic nanoparticles suspended in liquid streamed in co-axially swirled disks," *Nanomaterials*, vol. 12, no. 4, p. 671, 2022.
- [20] S. Bilal, M. Imtiaz Shah, N. Z. Khan, A. Akgül, and K. S. Nisar, "Onset about non-isothermal flow of Williamson liquid over exponential surface by computing numerical simulation in perspective of Cattaneo Christov heat flux theory," *Alexandria Engineering Journal*, vol. 61, no. 8, pp. 6139–6150, 2022.
- [21] S. Bilal, I. A. Shah, A. Akgül et al., "Finite difference simulations for magnetically effected swirling flow of Newtonian liquid induced by porous disk with inclusion of thermophoretic particles diffusion," *Alexandria Engineering Journal*, vol. 61, no. 6, pp. 4341–4358, 2022.
- [22] M. M. Rahman, M. A. Alim, and M. A. H. Mamun, "Finite element analysis of mixed convection in a rectangular cavity with a heat-conducting horizontal circular cylinder,"

- Nonlinear Analysis Modelling and Control*, vol. 14, no. 2, pp. 217–247, 2009.
- [23] H. S. Majdi, A. M. Abed, and L. J. Habeeb, “Mixed convection heat transfer of CuO-H₂O nanofluid in a triangular lid-driven cavity with circular inner body,” *J. Mech. Eng. Res. and Dev.* vol. 44, no. 1, pp. 164–175, 2021.
- [24] M. S. Ishak, A. I. Alsabery, I. Hashim, and A. J. Chamkha, “Entropy production and mixed convection within trapezoidal cavity having nanofluids and localised solid cylinder,” *Scientific Reports*, vol. 11, no. 1, pp. 14700–14722, 2021.
- [25] A. M. Aly, M. Asai, and A. J. Chamkha, “Analysis of unsteady mixed convection in lid-driven cavity included circular cylinders motion using an incompressible smoothed particle hydrodynamics method,” *International Journal of Numerical Methods for Heat and Fluid Flow*, vol. 25, no. 8, pp. 2000–2021, 2015.
- [26] S. Bilal, N. Z. Khan, I. A. Shah, J. Awrejcewicz, A. Akgül, and M. B. Riaz, “Heat and flow control in cavity with cold circular cylinder placed in non-Newtonian fluid by performing finite element simulations,” *Coatings*, vol. 12, no. 1, p. 16, 2021.
- [27] N. Z. Khan, R. Mahmood, S. Bilal et al., “Mixed convective thermal transport in a lid-driven square enclosure with square obstacle,” *Alexandria Engineering Journal*, 2022.
- [28] I. A. Shah, S. Bilal, S. Noeiaghdam, U. Fernandez-Gamiz, and H. Shahzad, “Thermosolutal natural convection energy transfer in magnetically influenced Casson fluid flow in hexagonal enclosure with fillets,” *Results in Engineering*, vol. 15, p. 100584, Article ID 100584, 2022.
- [29] S. Bansal and D. Chatterjee, “Magneto-convective transport of nanofluid in a vertical lid-driven cavity including a heat-conducting rotating circular cylinder,” *Numerical Heat Transfer, Part A: Applications*, vol. 68, no. 4, pp. 411–431, 2015.
- [30] F. Selimefendigil and H. F. Öztop, “Numerical study of MHD mixed convection in a nanofluid filled lid driven square enclosure with a rotating cylinder,” *International Journal of Heat and Mass Transfer*, vol. 78, pp. 741–754, 2014.
- [31] L. K. Malla, S. K. Jena, S. K. Mahapatra, and A. J. Chamkha, “Mixed convection inside a fluid-porous composite cavity with centrally rotating cylinder,” *Heat Transfer - Asian Research*, vol. 47, no. 4, pp. 684–701, 2018.
- [32] M. M. Ali, M. A. Alim, and S. S. Ahmed, “Oriented magnetic field effect on mixed convective flow of nanofluid in a grooved channel with internal rotating cylindrical heat source,” *International Journal of Mechanical Sciences*, vol. 151, pp. 385–409, 2019.
- [33] W. Al-Kouz, B. A. I. Bendrer, A. Aissa et al., “Galerkin finite element analysis of magneto two-phase nanofluid flowing in double wavy enclosure comprehending an adiabatic rotating cylinder,” *Scientific Reports*, vol. 11, no. 1, pp. 16494–16508, 2021.
- [34] K. M. Gangawane and B. Manikandan, “Laminar natural convection characteristics in an enclosure with heated hexagonal block for non-Newtonian power law fluids,” *Chinese Journal of Chemical Engineering*, vol. 25, no. 5, pp. 555–571, 2017.
- [35] M. Sheikholeslami, I. Khan, and I. Tlili, “Non-equilibrium model for nanofluid free convection inside a porous cavity considering Lorentz forces,” *Scientific Reports*, vol. 8, no. 1, pp. 16881–16893, 2018.
- [36] A. Alhashash, “Free convection from a corrugated heated cylinder with nanofluids in a porous enclosure,” *Advances in Mechanical Engineering*, vol. 12, no. 8, Article ID 168781402095221, 2020.
- [37] T. Tayebi and A. J. Chamkha, “Magneto-hydrodynamic natural convection heat transfer of hybrid nanofluid in a square enclosure in the presence of a wavy circular conductive cylinder,” *Journal of Thermal Science and Engineering Applications*, vol. 12, no. 3, 2020.
- [38] M. A. Ismael, “Numerical solution of mixed convection in a lid-driven cavity with arc-shaped moving wall,” *Engineering Computations*, vol. 34, no. 3, pp. 869–891, 2017.
- [39] F. H. Ali, H. K. Hamzah, and A. Abdulkadhim, “Numerical study of mixed convection nanofluid in an annulus enclosure between outer rotating cylinder and inner corrugation cylinder,” *Heat Transfer - Asian Research*, vol. 48, no. 1, pp. 343–360, 2019.
- [40] H. K. Hamzah, F. H. Ali, M. Hatami, D. Jing, and M. Y. Jabbar, “Magnetic nanofluid behavior including an immersed rotating conductive cylinder: finite element analysis,” *Scientific Reports*, vol. 11, no. 1, pp. 4463–4483, 2021.
- [41] K. Mehmood, S. Hussain, and M. Sagheer, “Mixed convection in alumina-water nanofluid filled lid-driven square cavity with an isothermally heated square blockage inside with magnetic field effect: introduction,” *International Journal of Heat and Mass Transfer*, vol. 109, pp. 397–409, 2017.
- [42] S. Y. Motlagh and H. Soltanipour, “Natural convection of Al₂O₃-water nanofluid in an inclined cavity using Buongiorno’s two-phase model,” *International Journal of Thermal Sciences*, vol. 111, pp. 310–320, 2017.
- [43] M. A. Sheremet, H. F. Öztop, I. Pop, and K. Al-Salem, “MHD free convection in a wavy open porous tall cavity filled with nanofluids under an effect of corner heater,” *International Journal of Heat and Mass Transfer*, vol. 103, pp. 955–964, 2016.
- [44] M. Sathiyamoorthy and A. J. Chamkha, “Natural convection flow under magnetic field in a square cavity for uniformly (or) linearly heated adjacent walls,” *International Journal of Numerical Methods for Heat and Fluid Flow*, vol. 22, no. 5, pp. 677–698, 2012.
- [45] S. Das, R. N. Jana, and O. D. Makinde, “Mixed convective magneto-hydrodynamic flow in a vertical channel filled with nanofluids,” *Engineering Science and Technology, an International Journal*, vol. 18, no. 2, pp. 244–255, 2015.
- [46] B. C. Pak and Y. I. Cho, “Hydrodynamic and heat transfer study of dispersed fluids with submicron metallic oxide particles,” *Experimental Heat Transfer*, vol. 11, no. 2, pp. 151–170, 1998.
- [47] J. C. Maxwell, *A Treatise on Electricity and Magnetism*, Vol. 1, Clarendon Press, , Oxford, UK, 1873.
- [48] W. Cui, Z. Shen, J. Yang, and S. Wu, “Modified prediction model for thermal conductivity of spherical nanoparticle suspensions (nanofluids) by introducing static and dynamic mechanisms,” *Industrial & Engineering Chemistry Research*, vol. 53, no. 46, pp. 18071–18080, 2014.
- [49] A. Mahmoudi, I. Mejri, M. A. Abbassi, and A. Omri, “Analysis of the entropy generation in a nanofluid-filled cavity in the presence of magnetic field and uniform heat generation/absorption,” *Journal of Molecular Liquids*, vol. 198, pp. 63–77, 2014.
- [50] B. Ghasemi, S. M. Aminossadati, and A. Raisi, “Magnetic field effect on natural convection in a nanofluid-filled square enclosure,” *International Journal of Thermal Sciences*, vol. 50, no. 9, pp. 1748–1756, 2011.
- [51] H. F. Öztop and E. Abu-Nada, “Numerical study of natural convection in partially heated rectangular enclosures filled with nanofluids,” *International Journal of Heat and Fluid Flow*, vol. 29, no. 5, pp. 1326–1336, 2008.

- [52] R. Nasrin, M. A. Alim, and A. J. Chamkha, "Buoyancy-driven heat transfer of water-Al₂O₃ nanofluid in a closed chamber: effects of solid volume fraction, Prandtl number and aspect ratio," *International Journal of Heat and Mass Transfer*, vol. 55, no. 25-26, pp. 7355–7365, 2012.
- [53] O. C. Zienkiewicz and R. L. Taylor, *The Finite Element Method*, McGraw-Hill, USA, 1991.
- [54] J. N. Reddy, *An Introduction to Finite Element Analysis*, McGraw-Hill, New York, 1993.
- [55] O. C. Zienkiewicz, R. L. Taylor, and J. M. Too, "Reduced integration technique in general analysis of plates and shells," *International Journal for Numerical Methods in Engineering*, vol. 3, no. 2, pp. 275–290, 1971.
- [56] M. M. Ali, R. Akhter, and M. A. Alim, "MHD natural convection and entropy generation in a grooved enclosure filled with nanofluid using two-component non-homogeneous model," *SN Applied Sciences*, vol. 2, no. 4, pp. 571–595, 2020.
- [57] R. Akhter, M. Mokaddes Ali, and M. A. Alim, "Entropy generation due to hydromagnetic buoyancy-driven hybrid-nanofluid flow in partially heated porous cavity containing heat conductive obstacle," *Alexandria Engineering Journal*, vol. 62, pp. 17–45, 2023.
- [58] C. Taylor and P. Hood, "A numerical solution of the Navier-Stokes equations using the finite element technique," *Computers & Fluids*, vol. 1, pp. 73–100, 1973.
- [59] P. Dechaumphai, *Finite Element Method in Engineering*, Chulalongkorn Uni.Press, Bangkok, 1999.
- [60] A. M. Rashad, M. A. Mansour, T. Armaghani, and A. J. Chamkha, "MHD mixed convection and entropy generation of nanofluid in a lid-driven U-shaped cavity with internal heat and partial slip," *Physics of Fluids*, vol. 31, no. 4, p. 042006, Article ID 042006, 2019.
- [61] K. M. Khanafer and A. J. Chamkha, "Mixed convection flow in a lid-driven enclosure filled with a fluid-saturated porous medium," *International Journal of Heat and Mass Transfer*, vol. 42, no. 13, pp. 2465–2481, 1999.
- [62] R. Iwatsu, J. M. Hyun, and K. Kuwahara, "Mixed convection in a driven cavity with a stable vertical temperature gradient," *International Journal of Heat and Mass Transfer*, vol. 36, no. 6, pp. 1601–1608, 1993.
- [63] R. Du, P. Gokulavani, M. Muthamilselvan, F. Al-Amri, and B. Abdalla, "Influence of the Lorentz force on the ventilation cavity having a centrally placed heated baffle filled with the Cu– Al₂O₃– H₂O hybrid nanofluid," *International Communications in Heat and Mass Transfer*, vol. 116, p. 104676, Article ID 104676, 2020.
- [64] A. H. Pordanjani, A. Jahanbakhshi, A. Ahmadi Nadooshan, and M. Afrand, "Effect of two isothermal obstacles on the natural convection of nanofluid in the presence of magnetic field inside an enclosure with sinusoidal wall temperature distribution," *International Journal of Heat and Mass Transfer*, vol. 121, pp. 565–578, 2018.